

Galaxy shape statistics in the effective field theory

Zvonimir Vlah^[a,b,c], Nora Elisa Chisari^[d], Fabian Schmidt^[e]

^aKavli Institute for Cosmology, University of Cambridge, Cambridge CB3 0HA, UK.

^bDepartment of Applied Mathematics and Theoretical Physics, University of Cambridge, Cambridge CB3 0WA, UK.

^cTheory Department, CERN, 1 Esplanade des Particules, CH-1211 Genève 23, Switzerland.

^dInstitute for Theoretical Physics, Utrecht University, Princetonplein 5, 3584 CC Utrecht, The Netherlands.

^eMax-Planck-Institut für Astrophysik, Karl-Schwarzschild-Str. 1, 85741 Garching, Germany.

E-mail: zv217@cam.ac.uk, n.e.chisari@uu.nl, fabians@mpa-garching.mpg.de

Abstract. Intrinsic galaxy alignments yield an important contribution to the observed statistics of galaxy shapes. The general bias expansion for galaxy sizes and shapes in three dimensions has been recently described by Vlah, Chisari & Schmidt using the general perturbative effective field theory (EFT) framework, in analogy to the clustering of galaxies. In this work, we present a formalism that uses the properties of spherical tensors to project galaxy shapes onto the observed sky in the flat-sky approximation, and compute the two-point functions at next-to-leading order as well as the leading-order three-point functions of galaxy shapes and number counts. The resulting expressions are given in forms that are convenient for efficient numerical implementation. For a source redshift distribution typical of Stage IV surveys, we find that that nonlinear intrinsic alignment contributions to galaxy shape correlations become relevant at angular wavenumbers $l \gtrsim 100$.

Contents

1	Introduction	1
2	EFT of intrinsic galaxy shapes	3
2.1	Galaxy shapes and bias expansion	3
2.2	Two-point functions in 3D	5
2.3	Three-point functions in 3D	6
3	Statistics of shape fields projected on the sky	7
4	Angular power spectra	10
4.1	Two-point functions	11
4.2	Three-point functions	13
5	Results for one-loop power spectrum and tree-level bispectrum	16
6	Conclusions	22
A	Gravitational lensing	23
B	Angular power spectrum	24
C	Angular bispectrum	26

1 Introduction

The advent of wide and fast galaxy surveys has triggered an era of precision cosmology from the large-scale structure, with this cosmological tool being used to elucidate the nature of the dark components of the Universe and the physics of the early Universe, among other goals. But in order for the inferences drawn from ever more powerful data sets to be robust, a similar progression must occur on the modelling side: our model for the observables needs to be accurate enough to guarantee no residual biases in the analyses.

Weak gravitational lensing is one of the phenomena observed in the large-scale structure which can yield information about the nature of dark matter and the origin of the accelerated expansion of the Universe. Gravitational lensing by the large-scale structure of the Universe distorts the shapes of background sources (galaxies) in a correlated manner. Although the signal is challenging to extract (amounting to percent-level correlated changes in galaxy ellipticities), it is now regularly and successfully extracted from multiple data sets, and a number of collaborations have presented cosmological constraints from this probe in the last decade [1–7].

One of the challenges in the modelling of galaxy shape correlations is the coherent distortion induced by gravitational interactions between galaxies and the large-scale distribution of matter in the Universe. Such physical distortions are known as “intrinsic alignments” and have been detected to high significance by multiple experiments, with an increasing body of work focusing on which, how and when galaxies align, and how these alignments give rise to a contamination of the weak lensing signal. On the other hand, their detection is on such

firm grounds [8–11] that there are proposals for their use as a cosmological probe on their own right [12–15].

So far, the modelling of intrinsic galaxy alignments has lagged behind similar efforts for other large-scale structure probes. The most commonly adopted model is the “linear alignment model” (LA) [16], which postulates a linear relation between the projected shapes of galaxies and the projected tidal field of the large-scale structure. This ansatz in any case provides a good description at large separations only. In the nonlinear regime, an excess above LA predictions is observed for early-type galaxies, which can be well-approximated by an *ad hoc* replacement of the linear matter power spectrum by its nonlinear analogue, while preserving the assumption of linear alignment [17]. An alternative for nonlinear modelling is the so-called “halo model”, by which the small-scale regime is modelled through the distribution of aligned central and satellite galaxies within a halo [18–20]. On the other hand, disk galaxies are assumed to be subject to alignments via tidal torques, and a separate set of models has been constructed to describe this flavor of alignments [21–23]. Cosmological simulations serve as a validation tool for all these models and help constrain their free parameters in as much as the simulated galaxy population is representative of the observed one [24–37].

The increasing precision of galaxy shape measurements requires, however, new modelling tools if we are to ensure the success of weak lensing cosmology [38]. Recently, a new theory approach was put forward that unifies the two alignment mechanisms under the same framework by means of standard perturbation theory (SPT) [39–41]. This more rigorous approach expands over the existing models and has already been applied to observational data sets [5, 42]. In [43], we presented a complete formulation that is based on a similar expansion in the context of the “effective field theory” (EFT) of the large-scale structure. Considering the symmetries of a trace-free tensor, we were able to identify all potential gravitational observables at a given order that contribute to describing any given biased tensorial tracer of the large-scale structure, including the intrinsic shapes of galaxies.

The EFT framework we presented in [43] focused on three-dimensional intrinsic shapes and their correlations. In this work, we connect the three-dimensional observables computed in that work to the projected ones from galaxy surveys, namely: quantities corresponding to the convergence field κ and shear fields γ_1 and γ_2 . We present results for the one-loop angular power spectrum and tree-level angular bispectrum for the convergence and shear auto- and cross-correlations. We emphasise, however, that the formalism derived in this work does not rely explicitly on the EFT expansion. Our findings can be applied to projecting the statistics of any three-dimensional scalar and tensorial fields regardless of how one chooses to model them. In this paper, we do not include nonlinear projection contributions, such as those from reduced shear. We will argue below that these are much smaller than the nonlinearities in intrinsic shape correlations which we treat here.

This work is organized as follows. In Section 2, we summarise the formalism presented in Paper I [43]. We define the projected observables in Section 3. We construct predictions for intrinsic alignment two-point and three-point correlations assuming the flat-sky approximation in Section 4. We produce numerical predictions for the typical observables and redshifts of galaxy surveys in Section 5. Conclusions are presented in Section 6. The contribution of gravitational lensing to the two-point shape statistics are included assuming the flat-sky approximation in Appendix A. Details of the projection calculation for the angular power spectrum are presented in Appendix B and similarly for the angular bispectrum in Appendix C.

δ_{ij}^K	Kronecker symbol
$\delta^D(\mathbf{x})$	Dirac delta function
$\mathcal{D}_{ij} \equiv \partial_i \partial_j / \partial^2 - (1/3) \delta_{ij}^K$	Shear derivative
$\mathbf{k}_{1\dots n} \equiv \mathbf{k}_1 + \dots + \mathbf{k}_n$	Sum notation
$\mathbf{Y}_{ij}^{(m)}(\hat{\mathbf{k}})$	Rank-two spherical tensor basis in Fourier space
$\mathbf{M}_{ij}^{(m)}(\hat{\mathbf{r}})$	Rank-two spherical tensor basis in configuration space
$f(\mathbf{k}) \equiv \int d^3\mathbf{x} f(\mathbf{x}) e^{-i\mathbf{k}\cdot\mathbf{x}}$	Fourier transform
$\langle O(\mathbf{k}_1) \dots O(\mathbf{k}_n) \rangle'$	n -point correlator without momentum conservation ¹
δ_m	Fractional matter density perturbation
$\Pi_{ij}^{[1]} \equiv \mathcal{D}_{ij} \delta_m + (1/3) \delta_{ij}^K \delta_m$	Scaled Hessian of gravitational potential
v^i	Matter velocity field
δ_n	Fractional galaxy number density perturbation
δ_s	Fractional galaxy size density perturbation (trace of shape tensor)
S_{ij}	3D galaxy shape tensor
g_{ij}	Trace-free part of 3D galaxy shape tensor
γ_{ij}	Projected shape on the sky (trace-free part of projected shape tensor)
$\hat{\mathbf{r}}$	Unit vector along the line of sight
$\hat{\mathbf{n}}$	Fixed unit vector perpendicular to the flat sky plane

Table 1: List of notation and most important quantities used in this paper. Fields in Fourier space are understood to be integrated over repeated momentum variables.

Throughout the paper, we assume an Euclidean Λ CDM cosmology with $\Omega_m = 0.272$, $\Omega_b = 0.0455$, $n_s = 0.967$, $\sigma_8 = 0.807$ and $h = 0.704$. We work under the assumptions of adiabatic Gaussian perturbations and General Relativity. It is straightforward to include the impact of primordial non-Gaussianity following previous work [13]. In perturbative calculations, we always make the usual approximation of setting the n -th order growth factor $D^{(n)}(\tau)$ to $[D(\tau)]^n$.

2 EFT of intrinsic galaxy shapes

2.1 Galaxy shapes and bias expansion

The three-dimensional shapes of galaxies in their rest frame are spin-2 quantities that can be described in terms of a well-defined expansion in local gravitational observables. In Paper I [43], we assumed that, for each galaxy α , its light distribution is described by the symmetric

¹Explicitly, we write

$$\langle O(\mathbf{k}_1) \dots O(\mathbf{k}_n) \rangle = (2\pi)^3 \delta^D(\mathbf{k}_{1\dots n}) \langle O(\mathbf{k}_1) \dots O(\mathbf{k}_n) \rangle', \quad (1.1)$$

where the Dirac delta function ensures the total momentum conservation, and is a consequence of the statistical translation invariance.

second-moment tensor $I_{ij}(\mathbf{r}_\alpha)$ (i.e., an ellipsoid) and defined by the shape fluctuation field²

$$S_{ij}(\mathbf{r}) = g_{ij}(\mathbf{r}) + \frac{1}{3}\delta_s(\mathbf{r})\delta_{ij}^K, \quad (2.1)$$

where the trace-free tensor g_{ij} describes galaxy shape perturbations, and the scalar field δ_s , galaxy size perturbations. We presented a new EFT expansion for the former in Paper I [43], while the latter is described by the usual EFT of scalar biased tracers [44, 45] in complete analogy to the case of galaxy number counts. This formalism allowed us to provide expressions for the two-point correlations between the intrinsic galaxy shape field and other scalar fields up to next-to-leading order, for which we drew analogies with the EFT application to scalar quantities, such as the number density of biased tracers [44, 45]. Moreover, we presented three-point functions for these tracers at leading order. The EFT approach also shows that one has to allow for distinct bias parameters in the bias expansion for the trace (size) and the trace-free (shape) parts.

Explicitly, we expand the number counts δ_n , size fields δ_s , and shape fields g_{ij} in terms of local gravitational observables as follows

$$\begin{aligned} a \in \{n, s\} : \quad \delta_a(\mathbf{k}, \tau) &= \sum_O b_O^{(a)}(\tau) \text{tr}[O_{ij}](\mathbf{k}, \tau), \\ g_{ij}(\mathbf{k}, \tau) &= \sum_O b_O^{(g)}(\tau) \text{TF}[O_{ij}](\mathbf{k}, \tau), \end{aligned} \quad (2.2)$$

where tr and TF denote the trace and trace-free components of a tensor, respectively, and $[O]$ are renormalized operators while $b_O^{(a)}$ are the corresponding (renormalized) bias parameters. The expansion is not unique, but if the physical processes that determine the properties of the tracers are *local*, reference [44] showed that one possible complete basis is the one comprised of all scalar combinations of a set of operators $\Pi^{[n]}$, defined recursively starting from

$$\Pi_{ij}^{[1]}(\mathbf{r}, \tau) = \frac{2}{3\Omega_m \mathcal{H}^2} \partial_{x,i} \partial_{x,j} \Phi(\mathbf{r}, \tau) = \frac{1}{3} \delta_{ij}^K \delta_m + \mathcal{D}_{ij} \delta_m. \quad (2.3)$$

Note that Eq. (2.3) contains the leading gravitational observables at a given spacetime position \mathbf{r}, τ : namely, the matter density perturbation δ_m , and the scaled tidal field $\mathcal{D}_{ij} \delta_m$. In the case of shapes, the expansion must account for all possible trace-free tensor combinations, which in general results in more contributions at a given order than in the scalar (density) case.

The computation of correlations between biased tensorial and scalar fields can be simplified by considerations of isotropy. To this end, in Paper I [43] we proposed to decompose any given tensorial field in spherical tensors [46] of multipole order $\ell = 2$, whose transformation properties under rotation are known. We thus decompose the shape tensor field into these basis functions in terms of helicity $m = 0, \pm 1, \pm 2$ defined with respect to the wavevector \mathbf{k} :

$$\begin{aligned} S_{ij}(\mathbf{k}) &= \sum_{\ell=0,2} \sum_{m=-\ell}^{\ell} S_{\ell}^{(m)}(\mathbf{k}) \left(\mathbf{Y}_{\ell}^{(m)}(\hat{\mathbf{k}}) \right)_{ij} \\ &= \frac{1}{3} S_0^{(0)}(\mathbf{k}) \delta_{ij}^K Y^{(0)} + \sum_{m=-2}^2 S_2^{(m)}(\mathbf{k}) \mathbf{Y}_{ij}^{(m)}(\hat{\mathbf{k}}), \end{aligned} \quad (2.4)$$

²Different normalizations of the S_{ij} field are possible, though this does not affect the form or range of validity of the EFT expansion.

where $\mathbf{Y}_{0,ij}^{(0)} = Y^{(0)}\delta_{ij}^K$, and $Y^{(0)} = 1$ is the single scalar helicity-0 mode (explicitly written in this form for the purpose of symmetry). Hereafter, we will drop the tensor indices ℓ on the basis vectors and use the boldface symbol \mathbf{Y} in order to emphasize that we are dealing with a basis $\ell = 2$ tensor, while for the $\ell = 0$ component we will use the explicit form given in Eq. (2.2). Note that the spherical tensor components $S_0^{(0)}(\mathbf{k})$ and $S_2^{(m)}(\mathbf{k})$ can be directly obtained from S_{ij} by projections using the basis tensors.

To construct the basis explicitly, we start by defining an orthonormal basis of three-dimensional Euclidean space comprised of tensors

$$\mathbf{e}_1 = \frac{\mathbf{k} \times \hat{\mathbf{n}}}{|\mathbf{k} \times \hat{\mathbf{n}}|}, \quad \mathbf{e}_2 = \hat{\mathbf{k}} \times \mathbf{e}_1, \quad \mathbf{e}_k = \hat{\mathbf{k}}, \quad (2.5)$$

where $\hat{\mathbf{n}}$ can be chosen as the line of sight direction. With this basis defined, we are able to build our helicity basis,

$$\mathbf{e}^0 = \mathbf{e}_k, \quad \mathbf{e}^\pm = \mp \frac{1}{\sqrt{2}} (\mathbf{e}_1 \mp i\mathbf{e}_2). \quad (2.6)$$

As a consequence, the orthonormal tensor basis functions can be defined as

$$\mathbf{Y}_{ij}^{(0)} = N_0 \left(\hat{k}_i \hat{k}_j - \frac{1}{3} \delta_{ij}^K \right), \quad \mathbf{Y}_{ij}^{(\pm 1)} = N_1 \left(\hat{k}_j \mathbf{e}_i^\pm + \hat{k}_i \mathbf{e}_j^\pm \right), \quad \mathbf{Y}_{ij}^{(\pm 2)} = N_2 \mathbf{e}_i^\pm \mathbf{e}_j^\pm, \quad (2.7)$$

where the normalization is chosen as $N_{0,1,2} = \left\{ \sqrt{\frac{3}{2}}, \sqrt{\frac{1}{2}}, 1 \right\}$. $\mathbf{Y}_{ij}^{(m)}$ are trace-free, and complex conjugation gives $\mathbf{Y}_{ij}^{(m)*} = (-1)^m \mathbf{Y}_{ij}^{(-m)}$, while a similar relation holds for the basis $\{\mathbf{e}_\pm, \mathbf{e}_0\}$.

2.2 Two-point functions in 3D

In Paper I [43], we considered the auto-correlations of scalar and trace-free tensor fields, and their cross-correlation, defined as

$$\begin{aligned} \langle \delta_a(\mathbf{k}) \delta_b(\mathbf{k}') \rangle' &= (2\pi)^3 \delta_{\mathbf{k}+\mathbf{k}'}^D P^{ab}(k), \quad \text{where } a, b \in \{\text{n, s}\} \\ \langle \delta_a(\mathbf{k}) g_{ij}(\mathbf{k}') \rangle' &= (2\pi)^3 \delta_{\mathbf{k}+\mathbf{k}'}^D P_{ij}^{ag}(k) \\ \langle g_{ij}(\mathbf{k}) g_{kl}(\mathbf{k}') \rangle' &= (2\pi)^3 \delta_{\mathbf{k}+\mathbf{k}'}^D P_{ijkl}^{\text{gg}}(k). \end{aligned} \quad (2.8)$$

and we obtained explicit expressions for these by using the EFT expansion of the shape field (Eq. 2.2) and projecting out the trace and trace-free part of the power spectra. To simplify the calculation, we made use of the spherical tensor basis given in Eq. (2.4) and obtained these power spectra by combination of the ones corresponding to the spherical tensor field components $S_2^{(m)}$, which are invariant quantities that also transform as spherical tensors. For projecting onto the flat sky (Section 4), we can directly operate with the power spectra of the $S_2^{(m)}$ components, which we proceed to summarize in what follows.

Due to statistical isotropy and homogeneity, the component power spectra are given by

$$\left\langle S_\ell^{(m)}(\mathbf{k}) S_{\ell'}^{(m')}(\mathbf{k}') \right\rangle = (2\pi)^3 \delta_{m m'}^K \delta_{\mathbf{k}+\mathbf{k}'}^D P_{\ell \ell'}^{(m)}(k), \quad (2.9)$$

where $\ell, \ell' = 0, 2$ represent the trace and trace-free components, respectively, and m, m' are helicity components. Different helicity components do not correlate. This is a consequence of statistical isotropy. Because the shape tensor field is real, and we assume parity invariance, this implies that the power spectra of the helicity components must satisfy: $P_{\ell \ell'}^{(m)}(k) =$

$P_{\ell\ell'}^{(-m)}(k)$. As a consequence, the shape-shape tensor power spectrum can be decomposed into six independent contributions,

$$P_{ijkl}^{SS}(\mathbf{k}) = \frac{1}{9}\delta_{ij}^K\delta_{kl}^K P_{00}^{(0)}(k) + \frac{1}{3}\delta_{\{ij\}}^K \mathbf{Y}_{kl}^{(0)} P_{02}^{(0)}(k) + \mathbf{Y}_{ij}^{(0)} \mathbf{Y}_{kl}^{(0)} P_{22}^{(0)}(k) + \sum_{q=1}^2 (-1)^q \mathbf{Y}_{\{ij\}}^{(q)} \mathbf{Y}_{kl}^{(-q)} P_{22}^{(q)}(k), \quad (2.10)$$

where the last term is symmetrized over (q) and $(-q)$ contributions, and the curly brackets in the subscripts denote symmetrization over the two pairs of indices.

We are now able to take the trace or trace-free components to obtain expressions for the power spectra defined in Eq. (2.8), for which we obtain

$$\begin{aligned} P^{ab}(k) &= P_{00}^{ab(0)}(k), \quad \text{where } a, b \in \{n, s\} \\ P_{ij}^{ag}(\mathbf{k}) &= \mathbf{Y}_{ij}^{(0)}(\hat{\mathbf{k}}) P_{02}^{ag(0)}(k), \\ P_{ijkl}^{gg}(\mathbf{k}) &= \mathbf{Y}_{ij}^{(0)}(\hat{\mathbf{k}}) \mathbf{Y}_{kl}^{(0)}(\hat{\mathbf{k}}) P_{22}^{gg(0)}(k) + \sum_{q=1}^2 (-1)^q \mathbf{Y}_{\{ij\}}^{(q)}(\hat{\mathbf{k}}) \mathbf{Y}_{kl}^{(-q)}(\hat{\mathbf{k}}) P_{22}^{gg(q)}(k). \end{aligned} \quad (2.11)$$

Explicit expressions for the spherical component power spectra up to one-loop order in perturbation theory were provided in Section 5 of Paper I [43] relying on the EFT expansion. Nevertheless, the decomposition in spherical tensors that we presented in Paper I [43] and summarized here is valid nonlinearly for any order in PT.

2.3 Three-point functions in 3D

We now consider three tensor fields, each with a trace and trace-free part. The bispectrum of these fields is defined by

$$\langle S_{ij}(\mathbf{k}_1) S_{kl}(\mathbf{k}_2) S_{rs}(\mathbf{k}_3) \rangle = (2\pi)^3 \delta_{\mathbf{k}_1+\mathbf{k}_2+\mathbf{k}_3}^D B_{ijklrs}^{SSS}(\mathbf{k}_1, \mathbf{k}_2, \mathbf{k}_3), \quad (2.12)$$

Given the decomposition of S_{ij} into spherical tensor components (Eq. (2.4)), we can also define the bispectrum of a combination of the components as

$$\left\langle S_{\ell_1}^{(m_1)}(\mathbf{k}_1) S_{\ell_2}^{(m_2)}(\mathbf{k}_2) S_{\ell_3}^{(m_3)}(\mathbf{k}_3) \right\rangle = (2\pi)^3 \delta_{\mathbf{k}_1+\mathbf{k}_2+\mathbf{k}_3}^D B_{\ell_1\ell_2\ell_3}^{(m_1 m_2 m_3)}(\mathbf{k}_1, \mathbf{k}_2, \mathbf{k}_3). \quad (2.13)$$

As a result, the decomposition of the bispectrum in terms of the $\mathbf{Y}^{(m)}$ basis tensors is then

$$\begin{aligned} B_{ijklrs}^{SSS}(\mathbf{k}_1, \mathbf{k}_2, \mathbf{k}_3) &= \frac{1}{27} \delta_{ij}^K \delta_{kl}^K \delta_{rs}^K B_{000}^{(0,0,0)}(\mathbf{k}_1, \mathbf{k}_2, \mathbf{k}_3) \\ &+ \frac{1}{9} \delta_{ij}^K \delta_{kl}^K \sum_{m_3=-2}^2 \mathbf{Y}_{rs}^{(m_3)}(\hat{\mathbf{k}}_3) B_{002}^{(0,0,m_3)}(\mathbf{k}_1, \mathbf{k}_2, \mathbf{k}_3) + 2 \text{ cyc.} \\ &+ \frac{1}{3} \delta_{ij}^K \sum_{\substack{m_i=-2 \\ i=(2,3)}}^2 \mathbf{Y}_{kl}^{(m_2)}(\hat{\mathbf{k}}_2) \mathbf{Y}_{rs}^{(m_3)}(\hat{\mathbf{k}}_3) B_{022}^{(0,m_2,m_3)}(\mathbf{k}_1, \mathbf{k}_2, \mathbf{k}_3) + 2 \text{ cyc.} \\ &+ \sum_{\substack{m_i=-2 \\ i=(1,2,3)}}^2 \mathbf{Y}_{ij}^{(m_1)}(\hat{\mathbf{k}}_1) \mathbf{Y}_{kl}^{(m_2)}(\hat{\mathbf{k}}_2) \mathbf{Y}_{rs}^{(m_3)}(\hat{\mathbf{k}}_3) B_{222}^{(m_1,m_2,m_3)}(\mathbf{k}_1, \mathbf{k}_2, \mathbf{k}_3), \end{aligned} \quad (2.14)$$

with 2 cyclic permutations as indicated. Statistical rotation and parity invariance give additional requirements that these bispectra need to satisfy, namely

$$B_{\ell_1 \ell_2 \ell_3}^{(m_1, m_2, m_3)} = (-1)^{m_1 + m_2 + m_3} B_{\ell_1 \ell_2 \ell_3}^{(-m_1, -m_2, -m_3)}. \quad (2.15)$$

This significantly reduces the number of the independent bispectra of spherical tensor components in the expansion of Eq. (2.14).

The EFT framework developed in Paper I [43] allowed us to find all the independent contributions to each bispectrum $B_{\ell_1 \ell_2 \ell_3}^{(m_1, m_2, m_3)}$. We refer the reader to that work for the explicit expansion of the three-dimensional bispectra of galaxy densities, sizes and shapes. Here, we will show how these bispectra, generically Eq. (2.12), can be projected on the sky with the help of the spherical tensor decomposition of Eq. (2.14).

The observables we are interested in are auto- and cross-correlators of galaxy densities, sizes and shapes. As mentioned in Paper I [43], one should note that helicity ± 1 and ± 2 can in principle contribute to any of the bispectra where at least one shape field is correlated. This is due to symmetry constraints being less stringent in the bispectrum, when compared to the power spectrum.

3 Statistics of shape fields projected on the sky

In imaging surveys we usually do not have access to the 3D shape of galaxies that we have thus far been describing. We can measure only 2D images, obtained by projections of the 3D shapes on the sky plane. Thus, in order to connect our theoretical models with the measured shape γ_{ij} these sky-projections need to be taken into account. If we introduce the projector

$$\mathcal{P}_{ij}(\hat{\mathbf{r}}) \equiv \delta_{ij}^K - \hat{r}_i \hat{r}_j, \quad (3.1)$$

where $\hat{\mathbf{r}}$ is the direction pointing along the line of sight on the sky, we can write the total shape field on the sky as

$$\gamma_{ij}(\mathbf{r}^s, z) = \text{TF} [\mathcal{P}_{ik} \mathcal{P}_{jl} g_{kl}(\mathbf{r}[\mathbf{r}^s], z)] + \gamma_{G,ij}(\mathbf{r}[\mathbf{r}^s], z), \quad (3.2)$$

where $\gamma_{G,ij}$ denotes the weak lensing shear, and \mathbf{r}^s and \mathbf{r} are respectively the redshift space and real space coordinates.³ At linear order lensing shear can be simply added to the intrinsic shape, however this holds only at leading order. In general, the observed shape field is a nonlinear function of shear and intrinsic shape; we will discuss this issue below. We will not consider these nonlinear effects, but defer them to future work.

Considering thus only the projections of the intrinsic shape, and neglecting redshift-space distortions, we can define

$$\gamma_{I,ij}(\mathbf{r}, z) \equiv \text{TF} [\mathcal{P}_{ik} \mathcal{P}_{jl} g_{kl}(\mathbf{r}, z)] = \mathcal{P}_{ijkl}(\hat{\mathbf{r}}) g_{kl}(\mathbf{r}, z) \quad (3.3)$$

where we defined the total projecting operator

$$\mathcal{P}_{ijkl}(\hat{\mathbf{r}}) \equiv \mathcal{P}_{ik}(\hat{\mathbf{r}}) \mathcal{P}_{jl}(\hat{\mathbf{r}}) - \frac{1}{2} \mathcal{P}_{ij}(\hat{\mathbf{r}}) \mathcal{P}_{kl}(\hat{\mathbf{r}}), \quad (3.4)$$

³Note that the projectors \mathcal{P}_{ij} are invariant on the redshift space mapping, i.e.

$$\mathcal{P}_{ik}(\hat{\mathbf{r}}) = \mathcal{P}_{ik}(\hat{\mathbf{r}}^s),$$

since the directions of real and redshift space coordinates coincide.

Projector operators have a simple idempotent property $\mathcal{P}_{ij}\mathcal{P}_{jk} = \mathcal{P}_{ik}$ and are orthogonal to $\hat{r}_i\hat{r}_j$, but not to the isotropic term δ_{ik}^K .

To obtain the Fourier transform of $\gamma_{I,ij}(\mathbf{r}, z)$ field the following integral would have to be performed

$$\gamma_{I,ij}(\mathbf{k}, z) = \int d^3r e^{i\mathbf{r}\cdot\mathbf{k}} \gamma_{I,ij}(\mathbf{r}, z) = \int \frac{d^3p}{(2\pi)^3} \mathcal{P}_{ijkl}(\mathbf{k} - \mathbf{p}) g_{kl}(\mathbf{p}, z). \quad (3.5)$$

The mode coupling evidenced in the last equality is due to the fact that the projection operator breaks translation invariance. This issue is circumvented by performing the spherical harmonic decomposition on the sky, or the 2D Fourier transform in case when sufficiently small scales are considered (flat-sky approximation).

However, let us first decompose the configuration space tensor field $\gamma_{I,ij}$ into the irreducible spherical tensor components, similar to what we did in Fourier space in section 2.1. We can thus introduce the helicity basis $(\hat{\mathbf{r}}, \mathbf{m}_+, \mathbf{m}_-)$ in analogy to Eq. (2.5),

$$\mathbf{m}_1 = \frac{\mathbf{e}_x \times \hat{\mathbf{r}}}{|\mathbf{e}_x \times \hat{\mathbf{r}}|}, \quad \mathbf{m}_2 = \hat{\mathbf{r}} \times \mathbf{m}_1, \quad \mathbf{m}^\pm = \mp \frac{1}{\sqrt{2}} (\mathbf{m}_1 \mp i\mathbf{m}_2), \quad (3.6)$$

where \mathbf{e}_x is a fixed unit vector that is not parallel to $\hat{\mathbf{r}}$, and construct out of it the rank two harmonic tensor basis $\mathbf{M}_{ij}^{(\pm 2)} = m_i^\pm m_j^\pm$. Even though we could introduce the other elements of the basis $\mathbf{M}_{ij}^{(0)}$ and $\mathbf{M}_{ij}^{(\pm 1)}$ (defined in analogy to Eq. (2.7)) these would be orthogonal to the total projection operator \mathcal{P}_{ijkl} given in Eq. (3.4) and thus would not contribute to the decomposition of the projected shape $\gamma_{I,ij}$. The traceless intrinsic shape field can then be decomposed in terms of two components on the sky

$$\gamma_{I,ij}(\mathbf{r}, z) = \gamma_{+2}(\mathbf{r}, z) \mathbf{M}_{ij}^{(+2)}(\hat{\mathbf{r}}) + \gamma_{-2}(\mathbf{r}, z) \mathbf{M}_{ij}^{(-2)}(\hat{\mathbf{r}}). \quad (3.7)$$

An especially useful property of this basis is the realization that \mathbf{m}^\pm basis vectors are unit eigenfunctions of the projectors \mathcal{P}_{ij} , i.e. we have

$$\mathcal{P} \cdot \mathbf{m}^\pm = \mathbf{m}^\pm. \quad (3.8)$$

This implies that

$$\mathbf{M}_{ij}^{(\pm 2)*}(\hat{\mathbf{r}}) \mathcal{P}_{ijkl}(\hat{\mathbf{r}}) = m_i^\mp m_j^\mp \left(\mathcal{P}_{ik}(\hat{\mathbf{r}}) \mathcal{P}_{jl}(\hat{\mathbf{r}}) - \frac{1}{2} \mathcal{P}_{ij}(\hat{\mathbf{r}}) \mathcal{P}_{kl}(\hat{\mathbf{r}}) \right) = \mathbf{M}_{kl}^{(\pm 2)*}(\hat{\mathbf{r}}), \quad (3.9)$$

which combined with Eq. (3.3) gives the simple relation

$$\gamma_{\pm 2}(\mathbf{r}, z) = \mathbf{M}_{ij}^{(\pm 2)*}(\hat{\mathbf{r}}) g_{ij}(\mathbf{r}, z). \quad (3.10)$$

The components $\gamma_{\pm 2}$ transform under rotation as helicity-two functions, and we have $\gamma_s^*(\mathbf{r}) = (-1)^s \gamma_{-s}(\mathbf{r})$

If we integrate over the line of sight coordinate, introducing a window function $W(\chi)$ determined by the redshift distribution $dN(z)/dz$ of galaxies, we have

$$\gamma_{\pm 2}(\hat{\mathbf{r}}) \equiv \int d\chi W(\chi) \int d^3r' \gamma_{\pm 2}(\mathbf{r}', z[\chi]) \delta^D(\mathbf{r}' - \chi\hat{\mathbf{r}}) = \int d\chi W(\chi) \gamma_{\pm 2}(\chi\hat{\mathbf{r}}, z[\chi]), \quad (3.11)$$

where the variable χ is the comoving distance to redshift z .

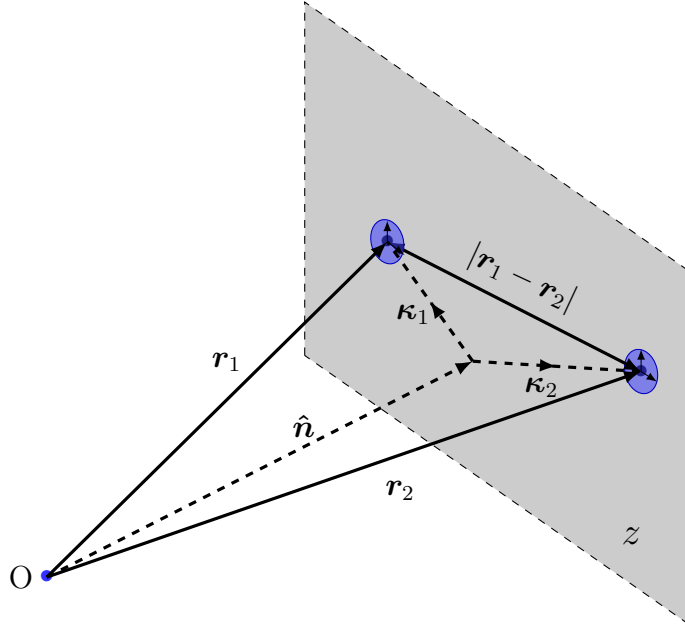


Figure 1: Coordinate setup in the flat sky approximation for the angular two-point functions. We use the coordinates labels where $\mathbf{r} = r_{\parallel} \hat{\mathbf{n}} + \boldsymbol{\kappa}$, with $r_{\parallel} = \hat{\mathbf{n}} \cdot \mathbf{r}$, and $\boldsymbol{\kappa}$ is the coordinate that lies in the observation plane, where we introduce the angular variable $\boldsymbol{\theta} = \boldsymbol{\kappa}/\chi$ (χ is the comoving distance at redshift z). The observer is assumed to be at the point O , and the observation plane is assumed to be at the distance determined by redshift z .

In surveys that do not cover a wide area of the sky, it is often useful and simpler to work in the *flat-sky* approximation. Here, the area on the sky is assumed to be well approximated by a plane lying perpendicular to a fixed direction $\hat{\mathbf{n}}$. This allows us to setup the coordinate frame where $\mathbf{r} = r_{\parallel} \hat{\mathbf{n}} + \boldsymbol{\kappa}$, with $r_{\parallel} = \hat{\mathbf{n}} \cdot \mathbf{r}$, $\boldsymbol{\kappa} = \mathbf{r} - r_{\parallel} \hat{\mathbf{n}}$, and $\boldsymbol{\theta} = \boldsymbol{\kappa}/\chi$. This coordinate setup is schematically shown in Figure 1. In this setting the integral over the redshift is performed along the line of sight $\hat{\mathbf{n}}$ and we have

$$\gamma_{\pm 2}(\boldsymbol{\theta}) \equiv \int d\chi W(\chi) \int d^3 r' \gamma_{\pm 2}(\mathbf{r}', z[\chi]) \delta^D(\mathbf{r}' - \chi \hat{\mathbf{n}} - \boldsymbol{\kappa}) = \int d\chi W(\chi) \gamma_{\pm 2}(\chi \hat{\mathbf{n}}, \chi \boldsymbol{\theta}, z[\chi]), \quad (3.12)$$

and the spherical tensors $\mathbf{M}_{ij}^{(\pm 2)}(\hat{\mathbf{n}})$ are also defined relative to the $\hat{\mathbf{n}}$ direction. Since we have established a 2D planar coordinate $\boldsymbol{\theta}$, we can also introduce a corresponding 2D Fourier transform. This is again useful, in the flat sky approximation, since the statistical isotropy can serve as an homogeneity condition on the plane and we can thus use statistical translation invariance. We thus define a Fourier field on a plane

$$\gamma_{I,ij}(\boldsymbol{\ell}) = \int d^2 \boldsymbol{\theta} \gamma_{I,ij}(\boldsymbol{\theta}) e^{i\boldsymbol{\ell} \cdot \boldsymbol{\theta}}. \quad (3.13)$$

and the decomposition in spherical tensors defined in the $\boldsymbol{\ell}$ plane orthogonal to the line of sight $\hat{\mathbf{r}}$ is

$$\gamma_{I,ij}(\boldsymbol{\ell}) = \gamma_{+2}(\boldsymbol{\ell}) \widetilde{\mathbf{M}}_{ij}^{(+2)}(\hat{\mathbf{n}}) + \gamma_{-2}(\boldsymbol{\ell}) \widetilde{\mathbf{M}}_{ij}^{(-2)}(\hat{\mathbf{n}}). \quad (3.14)$$

The basis $\widetilde{\mathbf{M}}^{(\pm 2)}$ spans a 2D Fourier space while orthogonal to the $\hat{\mathbf{n}}$ direction. We can think of it as being constructed from vector basis $(\hat{\mathbf{n}}, \hat{\boldsymbol{\ell}}_+, \hat{\boldsymbol{\ell}}_-)$, analogously as we did in Eq. (2.5),

but with $\hat{\ell}_\pm$ referring to a fixed direction $\hat{\mathbf{n}}$. Each of the helicity components in this Fourier space is given by

$$\gamma_{\pm 2}(\boldsymbol{\ell}) = \widetilde{\mathbf{M}}_{ij}^{(\pm 2)*}(\hat{\mathbf{n}})\gamma_{I,ij}(\boldsymbol{\ell}) = \int d^2\boldsymbol{\theta} \gamma_{\pm 2}(\boldsymbol{\theta})e^{\pm 2i(\phi_\theta - \phi_\ell)}e^{i\boldsymbol{\ell}\cdot\boldsymbol{\theta}}. \quad (3.15)$$

Note that it is not obvious that $\gamma_{\pm 2}(\boldsymbol{\ell})$, as defined above, will correspond to the small-angle limit of all sky treatment for high enough ℓ . However, this correspondence has been explicitly established in e.g. [47], by taking the small-angle limit of the all sky results, and we will return to it in our upcoming *all-sky* paper.

Very frequently, different bases for decomposing the $\gamma_{I,ij}$ are used in the literature. Some of the most prominent are the *polarization basis* (E, B) used in the study of the CMB polarization [48–50], and what we label the *Pauli basis* (γ_1, γ_2). The relation of our helicity basis to the polarization basis of galaxy shapes (γ_E, γ_B) is a simple linear combination

$$\gamma_E = \frac{1}{2}(\gamma_{+2} + \gamma_{-2}), \quad \gamma_B = -\frac{i}{2}(\gamma_{+2} - \gamma_{-2}), \quad (3.16)$$

with the inverse $\gamma_{\pm 2} = (\gamma_E \pm i\gamma_B)$. Since we deal with the simple linear combination of the fields, these relations hold in both all-sky and flat-sky, as well as in both angle and Fourier space of the flat-sky approximation. On the other hand Pauli basis can be obtained by similar linear combination and additional rotation around the azimuthal angle ϕ . We have

$$\gamma_1 = \frac{1}{2}(\gamma_{+2}e^{2i\phi} + \gamma_{-2}e^{-2i\phi}), \quad \gamma_2 = \frac{i}{2}(\gamma_{+2}e^{2i\phi} - \gamma_{-2}e^{-2i\phi}). \quad (3.17)$$

and the inverse is given by $\gamma_{\pm 2} = e^{\pm 2i\phi}(\gamma_1 \pm i\gamma_2)$, where $\phi = \phi_\theta$ in real space and $\phi = \phi_\ell$ in Fourier space, denoting the azimuthal angles of $\boldsymbol{\theta}$ and $\boldsymbol{\ell}$, respectively. The Pauli basis can again be used either in all-sky or flat-sky, however it is more commonly used in the flat-sky case. As the name suggests, on the 2D sky in this basis can be organized as the linear combination

$$g_{ij}(\boldsymbol{\theta}) = \begin{pmatrix} \gamma_1 & \gamma_2 \\ \gamma_2 & -\gamma_1 \end{pmatrix}_{ij} = \gamma_1(\boldsymbol{\theta})(\sigma_3)_{ij} + \gamma_2(\boldsymbol{\theta})(\sigma_1)_{ij}, \quad (3.18)$$

where $\boldsymbol{\sigma}_1$ and $\boldsymbol{\sigma}_3$ are the Pauli matrices (see e.g. [51]). The relation of the Pauli basis and polarization basis is related by the simple plane rotation by a $2\phi_\theta$ spin angle. Electric (E) and magnetic (B) components in angle space are then given by

$$\begin{aligned} \gamma_E(\boldsymbol{\theta}) &= \cos(2\phi_\theta)\gamma_1(\boldsymbol{\theta}) + \sin(2\phi_\theta)\gamma_2(\boldsymbol{\theta}), \\ \gamma_B(\boldsymbol{\theta}) &= -\sin(2\phi_\theta)\gamma_1(\boldsymbol{\theta}) + \cos(2\phi_\theta)\gamma_2(\boldsymbol{\theta}), \end{aligned} \quad (3.19)$$

and equivalent expressions, as already noted, hold in the 2D Fourier space.

4 Angular power spectra

In this part, we explore the two- and three-point statistics in the flat-sky approximation. The coordinate set-up is as described in the earlier section and as suggested for the two-point function in Figure 1. These results agree with the corresponding all-sky result in the small-angle (high ℓ) limit, as will be shown in an upcoming paper.

4.1 Two-point functions

We can evaluate the angular correlation function using Eq. (3.15). We are interested in the following correlators:

$$\begin{aligned}
\langle \delta_{\mathbf{n}}(\boldsymbol{\ell}_1) | \delta_{\mathbf{n}}^*(\boldsymbol{\ell}_2) \rangle &= \int d^2\boldsymbol{\theta}_1 d^2\boldsymbol{\theta}_2 \langle \delta_{\mathbf{n}}(\boldsymbol{\theta}_1) \delta_{\mathbf{n}}^*(\boldsymbol{\theta}_2) \rangle e^{i\boldsymbol{\ell}_1 \cdot \boldsymbol{\theta}_1 - i\boldsymbol{\ell}_2 \cdot \boldsymbol{\theta}_2}, \\
\langle \delta_{\mathbf{n}}(\boldsymbol{\ell}_1) | \gamma_{s_2}^*(\boldsymbol{\ell}_2) \rangle &= \int d^2\boldsymbol{\theta}_1 d^2\boldsymbol{\theta}_2 \langle \delta_{\mathbf{n}}(\boldsymbol{\theta}_1) \gamma_{s_2}^*(\boldsymbol{\theta}_2) \rangle e^{-is_2(\phi_{\boldsymbol{\theta}_2} - \phi_{\boldsymbol{\ell}_2})} e^{i\boldsymbol{\ell}_1 \cdot \boldsymbol{\theta}_1 - i\boldsymbol{\ell}_2 \cdot \boldsymbol{\theta}_2}, \\
\langle \gamma_{s_1}(\boldsymbol{\ell}_1) | \gamma_{s_2}^*(\boldsymbol{\ell}_2) \rangle &= \int d^2\boldsymbol{\theta}_1 d^2\boldsymbol{\theta}_2 \langle \hat{\gamma}_{s_1}(\boldsymbol{\theta}_1) \gamma_{s_2}^*(\boldsymbol{\theta}_2) \rangle e^{is_1(\phi_{\boldsymbol{\theta}_1} - \phi_{\boldsymbol{\ell}_1}) - is_2(\phi_{\boldsymbol{\theta}_2} - \phi_{\boldsymbol{\ell}_2})} e^{i\boldsymbol{\ell}_1 \cdot \boldsymbol{\theta}_1 - i\boldsymbol{\ell}_2 \cdot \boldsymbol{\theta}_2}.
\end{aligned} \tag{4.1}$$

We use the s variable to label the helicity states ± 2 , and we will refer to \tilde{s} as the sign of the helicity state, i.e. $\tilde{s} = s/|s|$. Here and throughout, we assume galaxy number counts $\delta_{\mathbf{n}}$ as the scalar observable we are correlating with. The expressions however are applicable generally to any such scalar (e.g., galaxy sizes δ_s).

We note again that in the flat-sky approximation statistical isotropy manifests itself as the translation invariance (and rotation invariance around the line of sight) of the correlators on the plane. This allows us to define simple spectral functions that depend only on the amplitude of the $\boldsymbol{\ell}$ -mode on the plane

$$\begin{aligned}
(2\pi)^2 \delta^{\text{D}}(\boldsymbol{\ell} - \boldsymbol{\ell}') C_{\text{nn}}(\ell) &= \langle \delta_{\mathbf{n}}(\boldsymbol{\ell}) | \delta_{\mathbf{n}}^*(\boldsymbol{\ell}') \rangle, \\
(2\pi)^2 \delta^{\text{D}}(\boldsymbol{\ell} - \boldsymbol{\ell}') C_{\text{n}\pm}(\ell) &= \langle \delta_{\mathbf{n}}(\boldsymbol{\ell}) | \gamma_{\pm 2}^*(\boldsymbol{\ell}') \rangle, \\
(2\pi)^2 \delta^{\text{D}}(\boldsymbol{\ell} - \boldsymbol{\ell}') C_{\pm\pm}(\ell) &= \langle \gamma_{\pm 2}(\boldsymbol{\ell}) | \gamma_{\pm 2}^*(\boldsymbol{\ell}') \rangle.
\end{aligned} \tag{4.2}$$

The explicit calculation of these angular power spectra is given in Appendix B. We use the standard approximation that the longitudinal modes $k_{\parallel} = \hat{\mathbf{n}} \cdot \mathbf{k}$ do not contribute noticeably to the angular spectra compared to the modes perpendicular to the plane, i.e. $k_{\parallel} \ll k_{\perp}$. Note that this approximation is not strictly necessary, it however becomes accurate in the same regime where the flat-sky approximation does, and greatly simplifies the resulting expressions. Using the resulting expressions given in Eq. (B.15) we obtain

$$\begin{aligned}
C_{\text{n}+}(\ell) = C_{\text{n}-}(\ell) &= \frac{1}{2} \int d\chi \frac{W_{\text{n}}(\chi) W_g(\chi)}{\chi^2} N_0 P_{02}^{(0)}(\ell/\chi), \\
C_{++}(\ell) = C_{--}(\ell) &= \frac{1}{8} \int d\chi \frac{W_g^2(\chi)}{\chi^2} \left(2N_0^2 P_{22}^{(0)}(\ell/\chi) + 8N_1^2 P_{22}^{(1)}(\ell/\chi) + N_2^2 P_{22}^{(2)}(\ell/\chi) \right), \\
C_{+-}(\ell) = C_{-+}(\ell) &= \frac{1}{8} \int d\chi \frac{W_g^2(\chi)}{\chi^2} \left(2N_0^2 P_{22}^{(0)}(\ell/\chi) - 8N_1^2 P_{22}^{(1)}(\ell/\chi) + N_2^2 P_{22}^{(2)}(\ell/\chi) \right),
\end{aligned} \tag{4.3}$$

where W_{n} and W_g denote the window functions corresponding to number counts and shapes, respectively, and we have the normalization constants $N_{0,1,2} = \left\{ \sqrt{\frac{3}{2}}, \sqrt{\frac{1}{2}}, 1 \right\}$ (related to the basis $\mathbf{Y}_{ij}^{(m)}$ in Eq. 2.7). Above, we allowed for the fact that the window functions for number density W_{n} and for shapes W_g can be different. Note that when using these flat-sky expressions, it is found to be a much better approximation to use $\ell \rightarrow \ell + 1/2$ in the arguments of $P_{ss'}^q(\ell/\chi)$ power spectra above (see e.g. [52]). With this correction, the estimated error of the approximation is reduced from $O(\ell^{-1})$ to $O(\ell^{-2})$.

We can also consider the angular spectra in different bases, introduced earlier. In the polarization basis, defined in Eq. (3.16), angular power spectra are

$$\begin{aligned}
C_{nE}(\ell) &= \frac{1}{2} \int d\chi \frac{W_n(\chi)W_g(\chi)}{\chi^2} N_0 P_{02}^{(0)}(\ell/\chi), \\
C_{EE}(\ell) &= \frac{1}{8} \int d\chi \frac{W_g^2(\chi)}{\chi^2} \left(2N_0^2 P_{22}^{(0)}(\ell/\chi) + N_2^2 P_{22}^{(2)}(\ell/\chi) \right) \\
C_{BB}(\ell) &= \int d\chi \frac{W_g^2(\chi)}{\chi^2} N_1^2 P_{22}^{(1)}(\ell/\chi).
\end{aligned} \tag{4.4}$$

The cross correlators of B -modes with E -modes or a scalar field vanish as a consequence of statistical parity invariance (see e.g. Paper I [43]): $C_{nB}(\ell) = C_{EB}(\ell) = 0$. The angular power spectra in the helicity basis γ_{\pm} and the polarization basis are related by

$$\begin{aligned}
C_{n+}(\ell) &= C_{n-}(\ell) = C_{nE}(\ell), \\
C_{++}(\ell) &= C_{--}(\ell) = C_{EE}(\ell) + C_{BB}(\ell), \\
C_{+-}(\ell) &= C_{-+}(\ell) = C_{EE}(\ell) - C_{BB}(\ell).
\end{aligned} \tag{4.5}$$

The Pauli basis is related to the polarization by simple rotation in the plane Eq. (3.19). Angular power spectra in this basis are

$$\begin{aligned}
C_{n\gamma_1}(\ell, \phi_\ell) &= \cos(2\phi_\ell) C_{nE}(\ell), \\
C_{n\gamma_2}(\ell, \phi_\ell) &= \sin(2\phi_\ell) C_{nE}(\ell), \\
C_{\gamma_1\gamma_1}(\ell, \phi_\ell) &= \cos(2\phi_\ell)^2 C_{EE}(\ell) + \sin(2\phi_\ell)^2 C_{BB}(\ell), \\
C_{\gamma_1\gamma_2}(\ell, \phi_\ell) &= \sin(2\phi_\ell) \cos(2\phi_\ell) (C_{EE}(\ell) - C_{BB}(\ell)), \\
C_{\gamma_2\gamma_2}(\ell, \phi_\ell) &= \sin(2\phi_\ell)^2 C_{EE}(\ell) + \cos(2\phi_\ell)^2 C_{BB}(\ell).
\end{aligned} \tag{4.6}$$

So far, all expressions included intrinsic contributions to shape correlations. The corresponding expressions including the leading lensing effect are given in Appendix A.

Let us now return to the issue of nonlinear projection contributions. Since the shape measurement process is nonlinear, and the galaxy shape field is weighted by the number density of source galaxies, Eq. (3.2) receives additional corrections. One such effect is that shapes are in fact measuring the reduced shear [53–55]. However there are also nonlinear effects which depend on the intrinsic shapes of galaxies [56–58]. Some examples of resulting contributions are

$$\gamma_{ij}(\mathbf{r}^s, z) \supset \delta_g \gamma_{G,ij}, \quad \kappa \text{TF} [\mathcal{P}_{ik} \mathcal{P}_{jl} g_{kl}(\mathbf{r}[\mathbf{r}^s], z)], \quad \gamma_{G,(im)} \text{TF} [\mathcal{P}_{mk} \mathcal{P}_{jl} g_{kl}(\mathbf{r}[\mathbf{r}^s], z)]. \tag{4.7}$$

where γ_G denotes the lensing contribution to the shape distortion. On the other hand, in terms of purely intrinsic contributions, the effect of number-density weighting is already included in our shape bias expansion, as explained in Paper I [43]. The contributions in Eq. (4.7) schematically add terms of the following form to angular shear correlations:

$$C_{EE}(\ell) \Big|_{\text{nonl. proj.}} \propto \int \frac{d^2 \ell'}{(2\pi)^2} C_{EE}^I(\ell') C_{EE}^G(|\ell - \ell'|). \tag{4.8}$$

That is, the convolution is performed after the projection. This is in contrast to the 1-loop shape contributions in Eq. (4.4), which involve the projection of a 3D convolution integral.

As shown in detail in [59], the latter contributions are much larger than the contributions from nonlinear projection effects. For this reason, we are justified in ignoring the latter here, even though they are formally of the same order in perturbations.

In terms of lensing contributions only, this hierarchy is well known: reduced-shear corrections to the shear power spectrum are much smaller than the corrections to the nonlinearities in the matter density field [55, 57, 58].

4.2 Three-point functions

We turn next to the angular bispectrum calculation in the flat-sky approximation. The details of the derivation are presented in Appendix C and here we give a summary of the results.

In analogy to how we define the flat-sky angular power spectrum in Eq. (4.9) we can define the angular bispectrum. We thus have

$$\begin{aligned}
(2\pi)^2 \delta^D(\ell_1 + \ell_2 + \ell_3) B_{\text{nnn}}(\ell_1, \ell_2, \ell_3) &= \langle \delta_{\text{n}}(\ell_1) \delta_{\text{n}}(\ell_2) \delta_{\text{n}}(\ell_3) \rangle, \\
(2\pi)^2 \delta^D(\ell_1 + \ell_2 + \ell_3) B_{\text{nn}\pm}(\ell_1, \ell_2, \ell_3) &= \langle \delta_{\text{n}}(\ell_1) \delta_{\text{n}}(\ell_2) \gamma_{\pm 2}(\ell_3) \rangle, \\
(2\pi)^2 \delta^D(\ell_1 + \ell_2 + \ell_3) B_{\text{n}\pm\pm}(\ell_1, \ell_2, \ell_3) &= \langle \delta_{\text{n}}(\ell_1) \gamma_{\pm 2}(\ell_2) \gamma_{\pm 2}(\ell_3) \rangle, \\
(2\pi)^2 \delta^D(\ell_1 + \ell_2 + \ell_3) B_{\pm\pm\pm}(\ell_1, \ell_2, \ell_3) &= \langle \gamma_{\pm 2}(\ell_1) \gamma_{\pm 2}(\ell_2) \gamma_{\pm 2}(\ell_3) \rangle.
\end{aligned} \tag{4.9}$$

To obtain the relation of these angular bispectra to the 3D spherical tensor bispectra in Section 2.3 in the flat-sky approximation we again use the approximation that the longitudinal modes $k_{\parallel} = \hat{\mathbf{n}} \cdot \mathbf{k}$ contribute negligibly to the perpendicular modes k_{\perp} that lay in the plane of the sky (see Figure 1). We thus assume that $k_{\parallel} \ll k_{\perp}$. We again note that relaxing this approximation would give rise to the subleading corrections in ℓ variables. However, with this approximation we ensure translation invariance in the plane manifested as the Dirac delta's on the left hand side of definitions in Eq. (4.9). We obtain the results given in Eq. (C.6) that we review here. The density-density-density angular bispectrum is given by

$$B_{\text{nnn}}(\ell_1, \ell_2, \ell_3) = \int d\chi \frac{[W_{\text{n}}(\chi)]^3}{\chi^4} B_{000}^{(0)}(\tilde{\ell}_1, \tilde{\ell}_2, \tilde{\ell}_3), \tag{4.10}$$

where we use the shorthand notation $\tilde{\ell} = \ell\chi$. This result is the standard clustering bispectrum [53].

The density-density-shape angular bispectrum is given by

$$B_{\text{nn}\pm}(\ell_1, \ell_2, \ell_3) = \frac{1}{2} \int d\chi \frac{[W_{\text{n}}(\chi)]^2 W_g(\chi)}{\chi^4} \left[N_0 B_{002}^{(0)} \mp i 2\sqrt{2} N_1 B_{002}^{(1)} - N_2 B_{002}^{(2)} \right] (\tilde{\ell}_1, \tilde{\ell}_2, \tilde{\ell}_3). \tag{4.11}$$

In the polarization basis introduced in Eq. (3.16), density-density-shape angular bispectrum can be split into E and B components yielding

$$\begin{aligned}
B_{\text{nn}E}(\ell_1, \ell_2, \ell_3) &= \frac{1}{2} \int d\chi \frac{[W_{\text{n}}(\chi)]^2 W_g(\chi)}{\chi^4} \left[N_0 B_{002}^{(0)} - N_2 B_{002}^{(2)} \right] (\tilde{\ell}_1, \tilde{\ell}_2, \tilde{\ell}_3), \\
B_{\text{nn}B}(\ell_1, \ell_2, \ell_3) &= -\sqrt{2} N_1 \int d\chi \frac{[W_{\text{n}}(\chi)]^2 W_g(\chi)}{\chi^4} B_{002}^{(1)}(\tilde{\ell}_1, \tilde{\ell}_2, \tilde{\ell}_3).
\end{aligned} \tag{4.12}$$

This decomposition has already been shown in Paper I [43] (see also [41] for similar results).

The density-shape-shape angular bispectrum in helicity basis can compactly be written as

$$\begin{aligned}
B_{n\tilde{s}_2\tilde{s}_3}(\ell_1, \ell_2, \ell_3) = & \frac{1}{8} \int d\chi \frac{W_n(\chi)[W_g(\chi)]^2}{\chi^4} \left[2N_0^2 B_{022}^{(0,0)} + 2s_2 s_3 N_1^2 \left(B_{022}^{(-1,1)} - B_{022}^{(1,1)} \right) \right. \\
& - i2\sqrt{2} N_0 N_1 \left(s_3 B_{022}^{(0,1)} + s_2 B_{022}^{(1,0)} \right) \\
& + i\sqrt{2} N_1 N_2 \left(s_2 B_{022}^{(1,2)} + s_3 B_{022}^{(2,1)} + s_3 B_{022}^{(-2,1)} + s_2 B_{022}^{(1,-2)} \right) \\
& \left. - 2N_0 N_2 B_{022}^{\{0,2\}} + N_2^2 \left(B_{022}^{(-2,2)} + B_{022}^{(2,2)} \right) \right] \left(\tilde{\ell}_1, \tilde{\ell}_2, \tilde{\ell}_3 \right). \tag{4.13}
\end{aligned}$$

It is important to notice that if we consider the cross-bispectrum (correlating at least two different shape tracers) we have four independent angular bispectra, since B_{n-+} can be different from B_{n+-} . In the case when only auto-bispectra (same tracers) are considered this simplifies and we have $B_{n-+} = B_{n+-}$. This can be seen if we consider the difference of the two angular bispectra. Using the explicit form above we have

$$\begin{aligned}
B_{n-+} - B_{n+-} = & -\frac{i}{\sqrt{2}} N_1 \int d\chi \frac{W_n(\chi)[W_g(\chi)]^2}{\chi^4} \left[2N_0 \left(B_{022}^{(1,0)} - B_{022}^{(0,1)} \right) \right. \\
& \left. + N_2 \left(B_{022}^{(1,-2)} - B_{022}^{(-2,1)} + B_{022}^{(1,2)} - B_{022}^{(2,1)} \right) \right], \tag{4.14}
\end{aligned}$$

which vanishes if the auto-correlation bispectrum is considered. This situation is intrinsically different from the case of power spectrum where $C_{+-} = C_{-+}$ (see Eq. 4.3) was guaranteed even for the cross correlations of different shape tracers. The reason for this lies in the fact that the imposed symmetries (statistical isotropy and parity invariance) are more constraining for the two-point functions, leaving less functional freedom than in case of three-point functions.

We can transform these results into the E and B basis to get

$$\begin{aligned}
B_{nEE}(\ell_1, \ell_2, \ell_3) = & \int d\chi \frac{W_n(\chi)[W_g(\chi)]^2}{4\chi^4} \left[N_0^2 B_{022}^{(0,0)} + N_0 N_2 B_{022}^{\{0,2\}} \right. \\
& \left. + \frac{N_2^2}{2} \left(B_{022}^{(-2,2)} + B_{022}^{(2,2)} \right) \right] \left(\tilde{\ell}_1, \tilde{\ell}_2, \tilde{\ell}_3 \right), \tag{4.15}
\end{aligned}$$

$$\begin{aligned}
B_{nEB}(\ell_1, \ell_2, \ell_3) = & N_1 \int d\chi \frac{W_n(\chi)[W_g(\chi)]^2}{2\sqrt{2}\chi^4} \left[-2N_0 B_{022}^{(0,1)} \right. \\
& \left. + N_2 \left(B_{022}^{(-2,1)} + B_{022}^{(2,1)} \right) \right] \left(\tilde{\ell}_1, \tilde{\ell}_2, \tilde{\ell}_3 \right),
\end{aligned}$$

$$\begin{aligned}
B_{nBE}(\ell_1, \ell_2, \ell_3) = & N_1 \int d\chi \frac{W_n(\chi)[W_g(\chi)]^2}{2\sqrt{2}\chi^4} \left[-2N_0 B_{022}^{(1,0)} \right. \\
& \left. + N_2 \left(B_{022}^{(1,-2)} + B_{022}^{(1,2)} \right) \right] \left(\tilde{\ell}_1, \tilde{\ell}_2, \tilde{\ell}_3 \right),
\end{aligned}$$

$$B_{nBB}(\ell_1, \ell_2, \ell_3) = N_1^2 \int d\chi \frac{W_n(\chi)[W_g(\chi)]^2}{\chi^4} \left[B_{022}^{(1,1)} + B_{022}^{(-1,1)} \right] \left(\tilde{\ell}_1, \tilde{\ell}_2, \tilde{\ell}_3 \right).$$

We again note that B_{nEB} and B_{nBE} are equal in the case of tracer auto-correlations, while in general they can be different when cross-correlating different tracers.

Finally, we turn to the correlations of the three shape fields. The general expression in terms of the helicity basis is given by

$$\begin{aligned}
B_{\tilde{s}_1\tilde{s}_2\tilde{s}_3}(\ell_1, \ell_2, \ell_3) = & \frac{1}{32} \int d\chi \frac{[W_g(\chi)]^3}{\chi^4} \left[4N_0^3 B_{222}^{(0,0,0)} - 4N_0^2 N_2 B_{222}^{\{\{0,0,2\}\}} \right. \\
& - N_2^3 \left(B_{222}^{\{\{-2,2,2\}\}} + B_{222}^{(2,2,2)} \right) \\
& + 4N_0 N_1^2 \left(s_2 s_3 \left(B_{222}^{(0,-1,1)} - B_{222}^{(0,1,1)} \right) + 2 \text{ cyc.} \right) \\
& + 2N_0 N_2^2 \left(B_{222}^{\{\{0,-2,2\}\}} + B_{222}^{\{\{0,2,2\}\}} \right) \\
& + 2N_1^2 N_2 \left(s_1 s_2 \left(B_{222}^{(1,1,2)} + B_{222}^{(1,1,-2)} - B_{222}^{\{\{-1,1,2\}\}} \right) + 2 \text{ cyc.} \right) \\
& - i4\sqrt{2} N_0^2 N_1 \left(s_3 B_{222}^{(0,0,1)} + 2 \text{ cyc.} \right) \\
& - i2\sqrt{2} s_1 s_2 s_3 N_1^3 \left(B_{222}^{\{\{-1,1,1\}\}} - B_{222}^{(1,1,1)} \right) \\
& - i\sqrt{2} N_1 N_2^2 \left(s_3 \left(B_{222}^{\{\{-2,2\},1\}} + B_{222}^{(2,2,1)} - B_{222}^{(2,2,-1)} \right) + 2 \text{ cyc.} \right) \\
& \left. + i2\sqrt{2} N_1 N_2 N_3 \left(s_3 \left(B_{222}^{\{\{0,-2\},1\}} + B_{222}^{\{\{0,2\},1\}} \right) + 2 \text{ cyc.} \right) \right] \left(\tilde{\ell}_1, \tilde{\ell}_2, \tilde{\ell}_3 \right).
\end{aligned} \tag{4.16}$$

As in case of the density shape-shape bispectra, we see that in the case where we are considering the single tracer auto-correlations, we have $B_{+--} = B_{-+-} = B_{-++}$, and similarly for the permutations of B_{+--} . Transforming these results into the E and B basis, we get

$$\begin{aligned}
B_{EEE}(\ell_1, \ell_2, \ell_3) = & \int d\chi \frac{W_n(\chi)[W_g(\chi)]^2}{32\chi^4} \left[4N_0^3 B_{222}^{(0,0,0)} - 4N_0^2 N_2 B_{222}^{\{\{0,0,2\}\}} \right. \\
& + 2N_0 N_2^2 \left(B_{222}^{\{\{0,-2,2\}\}} - B_{222}^{\{\{0,2,2\}\}} \right) \\
& \left. - N_2^3 \left(B_{222}^{\{\{-2,2,2\}\}} + B_{222}^{(2,2,2)} \right) \right] \left(\tilde{\ell}_1, \tilde{\ell}_2, \tilde{\ell}_3 \right), \\
B_{EEB}(\ell_1, \ell_2, \ell_3) = & -N_1 \int d\chi \frac{W_n(\chi)[W_g(\chi)]^2}{8\sqrt{2}\chi^4} \left[4N_0^2 B_{222}^{(0,0,1)} - 2N_0 N_2 \left(B_{222}^{\{\{0,-2,2\},1\}} + B_{222}^{\{\{0,2,2\},1\}} \right) \right. \\
& \left. + N_2^2 \left(B_{222}^{\{\{-2,2\},1\}} + B_{222}^{(2,2,1)} - B_{222}^{(2,2,-1)} \right) \right] \left(\tilde{\ell}_1, \tilde{\ell}_2, \tilde{\ell}_3 \right), \\
B_{EBB}(\ell_1, \ell_2, \ell_3) = & N_1^2 \int d\chi \frac{W_n(\chi)[W_g(\chi)]^2}{4\chi^4} \left[2N_0 \left(B_{222}^{(0,1,1)} - B_{222}^{(0,-1,1)} \right) \right. \\
& \left. + N_2 \left(B_{222}^{(2,\{-1,1\})} - B_{222}^{(2,1,1)} - B_{222}^{(-2,1,1)} \right) \right] \left(\tilde{\ell}_1, \tilde{\ell}_2, \tilde{\ell}_3 \right), \\
B_{BBB}(\ell_1, \ell_2, \ell_3) = & N_1^3 \int d\chi \frac{W_n(\chi)[W_g(\chi)]^2}{\sqrt{2}\chi^4} \left[B_{222}^{\{\{-1,1,1\}\}} - B_{222}^{(1,1,1)} \right] \left(\tilde{\ell}_1, \tilde{\ell}_2, \tilde{\ell}_3 \right).
\end{aligned} \tag{4.17}$$

Where, to obtain the values, for other cross-correlation components, like B_{EBE} etc., we need to take permutations of the $q = 1$ helicity index in $B_{222}^{(q_1, q_2, q_3)}$ bispectra in the expressions above. In case of auto correlations these are all equivalent again.

In Paper I [43], we presented the results for the 3D bispectra $B_{\ell_1, \ell_2, \ell_3}^{(q_1, q_2, q_3)}$ at tree level (LO - leading order) PT. We also showed explicitly the results for the density-density-shape angular bispectra, demonstrating that B_{nnE} both B_{nnB} contributions arise already at leading PT

order (see also [41]). For density-shape-shape and shape-shape-shape angular bispectra, the situation is different. At tree level, only one nonzero helicity q can contribute. This is because at leading order in PT, the $\Pi_{ij}(\mathbf{r})$ field given in Eq. (2.3) has only scalar contributions. The contributions that survive at leading order for all bispectra are then listed in Eq.(C.7) of Appendix C. We see that the $B_{n n E}$ and $B_{n n B}$ expressions given in Eq. (4.12) remain unchanged, while for the rest the number of contributions is substantially reduced. The expressions given in Eq. (4.15) at tree level thus reduce to

$$\begin{aligned} B_{nEE}(\ell_1, \ell_2, \ell_3) &= N_0 \int d\chi \frac{W_n(\chi)[W_g(\chi)]^2}{4\chi^4} \left[N_0 B_{022}^{(0,0)} + N_2 B_{022}^{\{\{0,2\}\}} \right] (\tilde{\ell}_1, \tilde{\ell}_2, \tilde{\ell}_3), \quad (4.18) \\ B_{nEB}(\ell_1, \ell_2, \ell_3) &= -N_0 N_1 \int d\chi \frac{W_n(\chi)[W_g(\chi)]^2}{\sqrt{2}\chi^4} B_{022}^{(0,1)} (\tilde{\ell}_1, \tilde{\ell}_2, \tilde{\ell}_3), \\ B_{nBB}(\ell_1, \ell_2, \ell_3) &= 0, \end{aligned}$$

where B_{nBE} is again equal to B_{nEB} in case of auto-correlations, while in case of cross-correlations in the expression above we need to replace the $B_{022}^{(0,1)}$ with $B_{022}^{(1,0)}$. Similarly, from Eq. (4.17) we get a substantial reduction of contributions

$$\begin{aligned} B_{EEE}(\ell_1, \ell_2, \ell_3) &= N_0^2 \int d\chi \frac{W_n(\chi)[W_g(\chi)]^2}{8\chi^4} \left[N_0 B_{222}^{(0,0,0)} - N_2 B_{222}^{\{\{0,0,2\}\}} \right] (\tilde{\ell}_1, \tilde{\ell}_2, \tilde{\ell}_3), \quad (4.19) \\ B_{EEB}(\ell_1, \ell_2, \ell_3) &= -N_0^2 N_1 \int d\chi \frac{W_n(\chi)[W_g(\chi)]^2}{2\sqrt{2}\chi^4} B_{222}^{(0,0,1)} (\tilde{\ell}_1, \tilde{\ell}_2, \tilde{\ell}_3), \\ B_{EBB}(\ell_1, \ell_2, \ell_3) &= B_{BBB}(\ell_1, \ell_2, \ell_3) = 0, \end{aligned}$$

and in case of the cross-correlations, B_{EBE} and B_{BEE} are given by helicity permutations of $B_{222}^{(0,0,1)}$, while the rest of the angular bispectra, involving more than one γ_B field are zero at tree-level.

5 Results for one-loop power spectrum and tree-level bispectrum

In this section we show the angular power spectrum and bispectrum of intrinsic galaxy shapes, based on the results obtained in Paper I [43]. As we indicated in the previous section we show the results using the flat-sky approximation. The primary motivation for this lies in the realization that on the scales where one-loop terms are relevant, flat-sky is a good approximation to the all-sky result. We will address the return to the all-sky results in the subsequent paper.

Before we continue, we would like to point out the issue of the redshift dependence of the free bias parameters. Generally, the bias parameters are expected to evolve on a Hubble time scale, so that one can write

$$b_O(z) = b_O(\bar{z}) + b'_O(\bar{z})(z - \bar{z}) + \dots \quad (5.1)$$

where b'_O is of similar order as b_O . If the redshift distribution considered is not too wide, then one can approximately work with constant bias parameters (the correction is of order $(\Delta z)^2$ where Δz is the width of the redshift distribution). We will however not explore this issue further in this paper and we thus assume that bias parameters are independent of redshift.

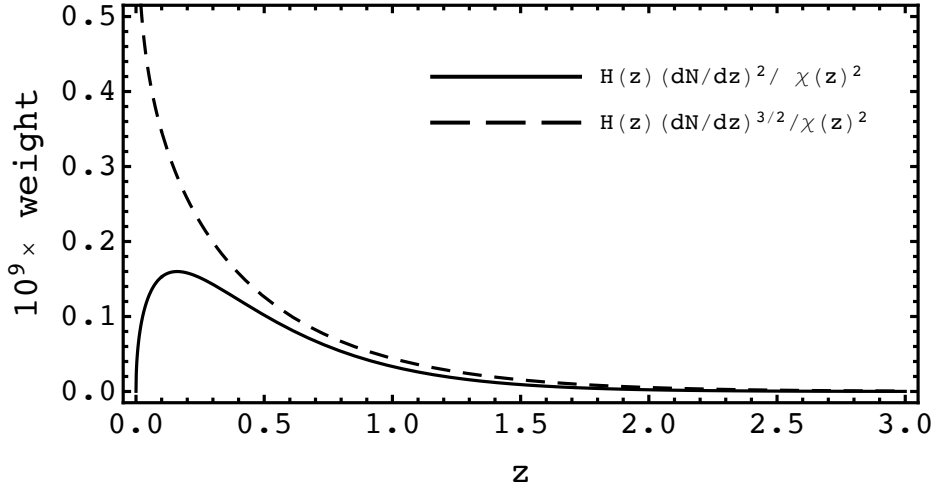


Figure 2: Power spectrum weight function (solid line) compared to the square root of the bispectrum weight function (dashed line), based on Eq. (5.3). Both weights are multiplied by the factor 10^9 . The dashed curve diverges at low redshifts as $z^{3/2\alpha-2}$.

Furthermore, in order to show some concrete results we assume a simple weight function $W_g(\chi)$ that corresponds to the redshift distribution of galaxies with shapes expected for a next generation wide and deep survey. In other words,

$$W_g(\chi) = \frac{dN}{dz} \frac{dz}{d\chi} \quad (5.2)$$

and where

$$\frac{dN}{dz} \propto z^\alpha \exp \left[- \left(\frac{z}{z_0} \right)^\beta \right], \quad \text{and} \quad \frac{dz}{d\chi} = H(z), \quad (5.3)$$

e.g. [38], where $\alpha = 1.24$, $\beta = 1.01$ and $z_0 = 0.51$. This specific example corresponds to the so-called “gold sample” of galaxies with shapes expected to be observed with the Rubin Observatory’s Legacy Survey of Space and Time [60, 61]. Note that the results shown here for shape correlations are for *intrinsic alignments alone*, i.e. without the contribution of the lensing signal. For simplicity, we assume that the same sample is used for both shapes and clustering, i.e. $W(\chi) \equiv W_n(\chi) = W_g(\chi)$. This is generally not the case in galaxy surveys, which tend to focus on either spectroscopic or color-selected clustering samples to achieve better redshift accuracy. Nevertheless, we adopt this simple case here for illustration purposes. In Figure 2 we show how these weight functions contribute to the angular power spectrum and bispectrum. We see that the weight function W_g^2 for the power spectrum peaks around the redshift $z \approx 0.2$, while in case of bispectrum the weight function W_g^3 (the square of what is shown in the figure) diverges at low redshifts as $\propto z^{3\alpha-4}$.

In Figure 3 we show the various cross and auto angular power spectra for galaxy number density and E and B -modes of galaxy shape. Below each sub-plot, we show the ratio between the terms obtained from the EFT one-loop prediction and the linear power spectrum. The exception is the bottom right case, since C_ℓ^{BB} is expected to be null at linear order. In this case, we normalize it to the EE power spectrum. The first angular power spectrum

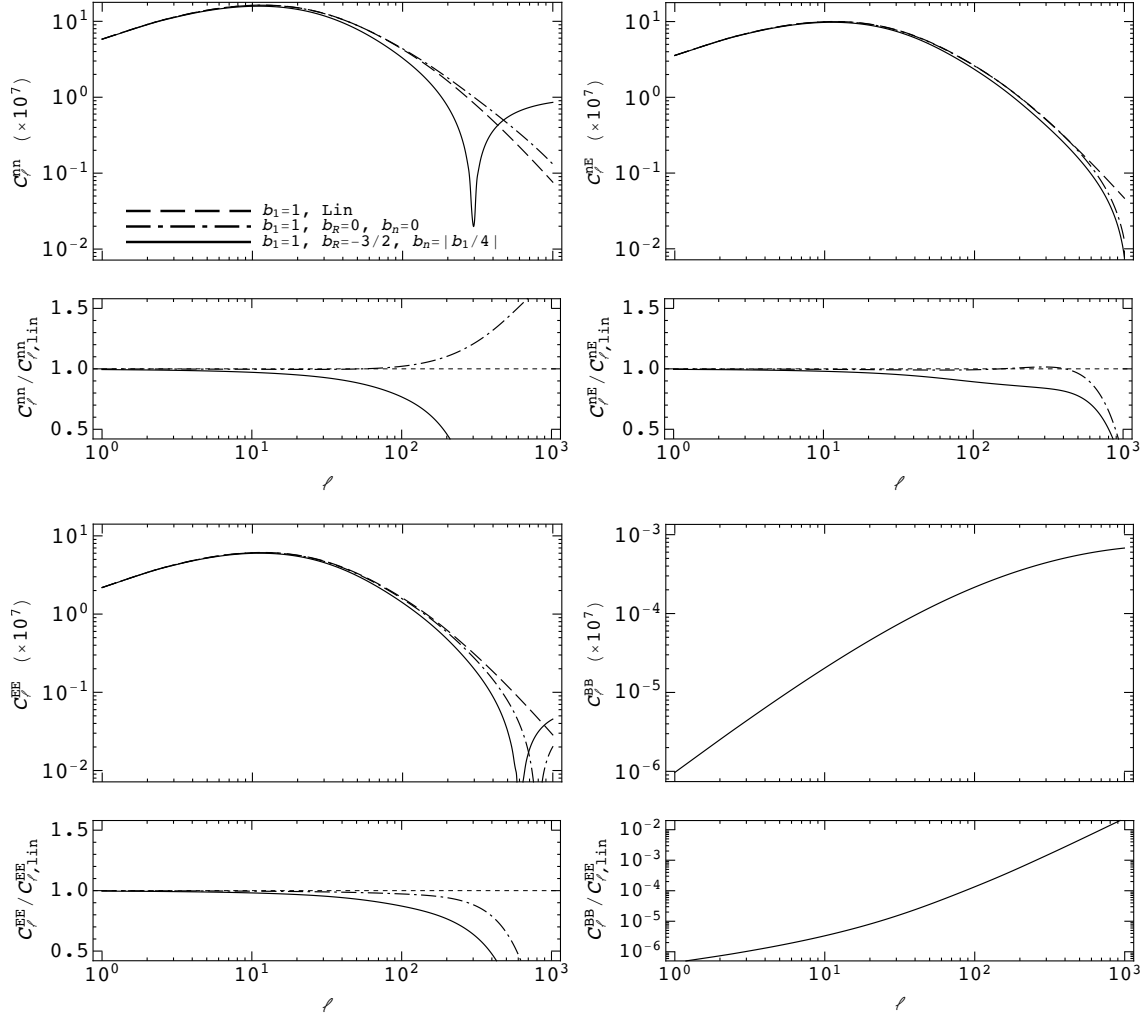


Figure 3: The angular density and shape auto- and cross- power spectra. In each panel, upper plots show the angular power spectra, while lower plots show the ratio to the linear theory. In the *upper-left* panel, we show the galaxy number density-number density contribution C_ℓ^{nn} . Dashed lines are linear theory predictions containing only b_1 bias parameter, dot-dashed lines are nonlinear predictions again using only b_1 bias parameter, while the solid lines show the full one-loop bias result. In the *upper-right* panel, we show galaxy number density- E -mode angular power spectrum C_ℓ^{nE} . Dashed, dot-dashed, and solid lines again correspond to contributions as in the previous panel. *Lower-left* panel shows the EE shape angular power spectrum, C_ℓ^{EE} , where again, three different lines are the same as in the previous panels. Lastly, the *lower-right* panel shows the BB shape angular power spectrum C_ℓ^{BB} . Here the leading order contributions start at one-loop with the characteristic mode coupling dependence at large scales that is highly suppressed relative to the $C_{EE,\text{lin}}$.

(upper-left panel) is the galaxy number density-number density contribution C_ℓ^{nn} . We plot the EFT contributions to the angular power spectra as given in Section 5.1 of Paper I [43]. We show three curves corresponding to: the linear bias with linear matter power spectrum (dashed line), the linear bias with the one-loop matter power spectrum (dot-dashed line),

and full EFT one-loop with non-linear biasing (solid line). In the last case we adopt the following values for the bias parameters: $b_1 = 1$, $b_{R_*} = -3/2$ and $b_n = b_1/4$ (all other bias coefficients), and we neglect the stochastic contributions. The adopted values for the bias parameters are chosen for visualization purposes only. In realistic cases, when the model is supposed to be contrasted with the data or simulations, these parameters would need to be fitted for. Similarly to this we show the contributions to the number density-shape angular power spectrum C_ℓ^{nE} (upper-right panel). Notice that the b_1 term in case of the shape spectra corresponds to the linear alignment model from [16]. From the ratio sub-plot shown below the C_ℓ^{nn} prediction, and in general for all other correlations shown in Figure 3, we see that the EFT contributions are scale-dependent and have the highest impact at the smallest separations between galaxies (large ℓ values), as expected. In practice, the EFT expansion should only be trusted as long as the new terms are a fraction of the linear one.

The bottom panels of Figure 3 show the intrinsic shape auto-correlations: C_ℓ^{EE} (left) and C_ℓ^{BB} (right), using the same bias value prescription. Our predictions indicate that C_ℓ^{BB} , which is null in linear alignment model predictions, is present at the mildly-nonlinear level. This is also in line with SPT predictions [40, 62]. However, because E and B -modes are connected by the same choice of biases, the bottom right panel of Figure 3 can be interpreted as the typical order of magnitude of B -modes at mildly non-linear scales in comparison to the E -modes. We find these to be highly suppressed.

In Figure 4, we show a plausible range for fractional contribution of one-loop terms to each linear angular power spectrum, as a function of multipole and based on the variation of bias parameters. The variation of the bias parameters corresponds to the choice given in Figure 3 of Paper I [43]. The three panels represent C_ℓ^{nn} , C_ℓ^{nE} and C_ℓ^{EE} . Note that we again neglect the stochastic bias contributions. The contributions are contained until scales of $l \sim 10^2$ and become comparable to the linear prediction for larger multipoles.

Since this paper is focused on intrinsic alignment contributions to galaxy shape correlations, we have not included the contribution from gravitational lensing here. Assuming that lensing and alignment effects are additive, which holds to leading order, it is straightforward to include gravitational lensing as described in Appendix A. The result for C_ℓ^{nE} shown here then functions as a contaminant to galaxy-galaxy lensing, while that for C_ℓ^{EE} is a contaminant to cosmic shear. Note however that there are also important cross-contributions of intrinsic alignments and lensing, which are included in the relations given in Appendix A.

Next, in Figure 5, we show the number density auto- and number density, number density and shape cross-bispectra. As mentioned, for all bispectra cases we adopt the simplification for the window function $W_g = W_n$, thus all the weights are proportional to W_g^3 . We adopt the same bias values as in the case of power spectra above. The tree-level 3D bispectra needed for the computation of the angular bispectra here are explicitly given in Section 5.2 of Paper I [43]. All panels are normalized by the maximal value attained over the configurations shown. In the upper panels we show the contributions for the number density auto-bispectrum B_{nnn} for configurations with maximal wavenumber $\ell_1 = 30$ (left panel) and $\ell_1 = 150$ (right panel). In both cases we see that the equilateral contributions are suppressed compared to the $\ell_2 + \ell_3 \approx \ell_1$ diagonal (flattened triangles), where the amplitude the bispectrum amplitudes reach their maximal values. Middle panel shows the number density, number density and E -mode cross-bispectrum B_{nnE} for the same maximal wavenumber ℓ_1 choices. We notice the similar relative configuration distribution as in the case of B_{nnn} , with the equilateral contributions suppressed relative to the $\ell_2 + \ell_3 \approx \ell_1$ diagonal. The property that the bispectrum amplitudes peak for the flattened triangles, where $\ell_2 + \ell_3 \approx \ell_1$, is in-

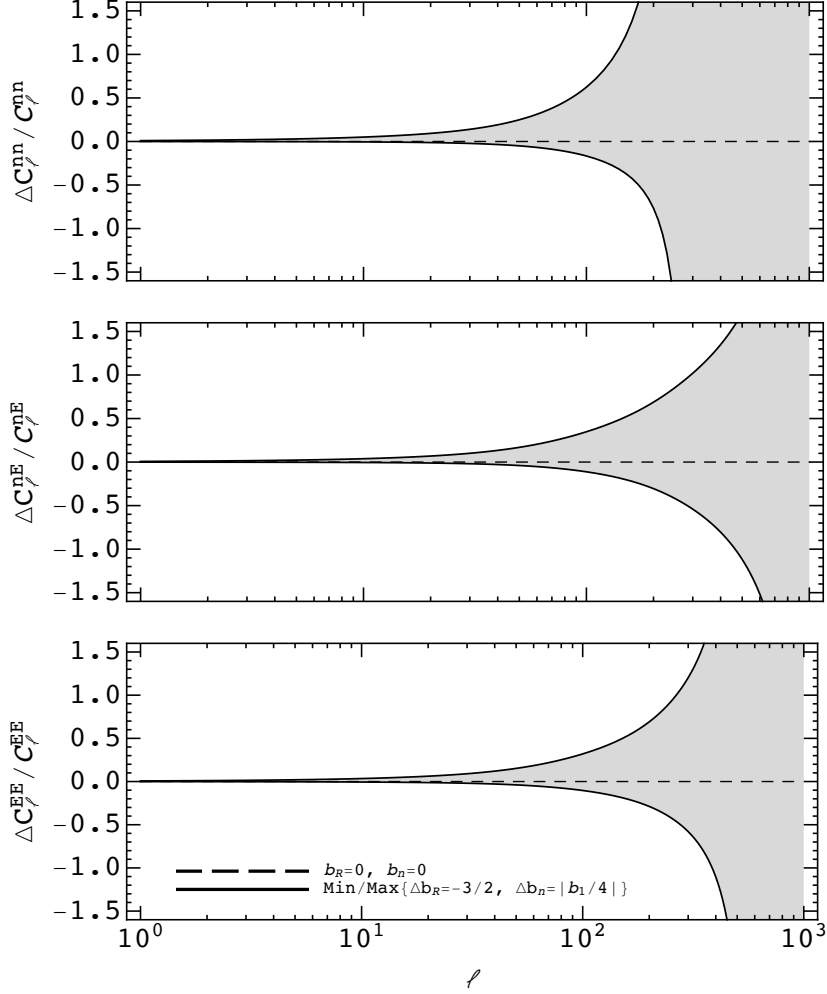


Figure 4: Relative one-loop bias contributions compared to the dark matter one-loop power spectra for C_ℓ^{nn} , C_ℓ^{nE} , C_ℓ^{EE} . We again use $b_1 = 1$, $b_{R^*} = -3/2$ and for the rest of the biases we use the values $|b_n| = b_1/4$. The sign of bias values b_n are adjusted so that the grey area represents the band of potential bias one-loop contributions where $|b_n| < b_1/4$. In all cases we neglect the stochastic bias contributions. Effectively this gives an estimate of the validity regime of linear alignment model, provided our bias coefficient choice is realistic.

herited from the similar behavior of the 3D bispectrum of matter and biased tracers (see the right panels of Fig. 10 in [45]).

Similar to the E -mode, in the lower panels we show the number density, number density and B -mode cross-bispectrum B_{nnB} . For the same choice of bias parameters as before, the maximal amplitude of this bispectrum is suppressed by an order of magnitude relative to the B_{nnn} and B_{nnE} . Additionally, relative to this maximal amplitude configuration, the rest of the configurations are further suppressed more strongly than in the B_{nnn} and B_{nnE} cases. In other words, in the B_{nnB} cross-bispectrum, most of the relevant contributions are roughly centered around the maximal amplitude configuration and they are again clustered close to the flattened triangle shapes, i.e. $\ell_2 + \ell_3 \approx \ell_1$ is diagonal. The latter feature can again be

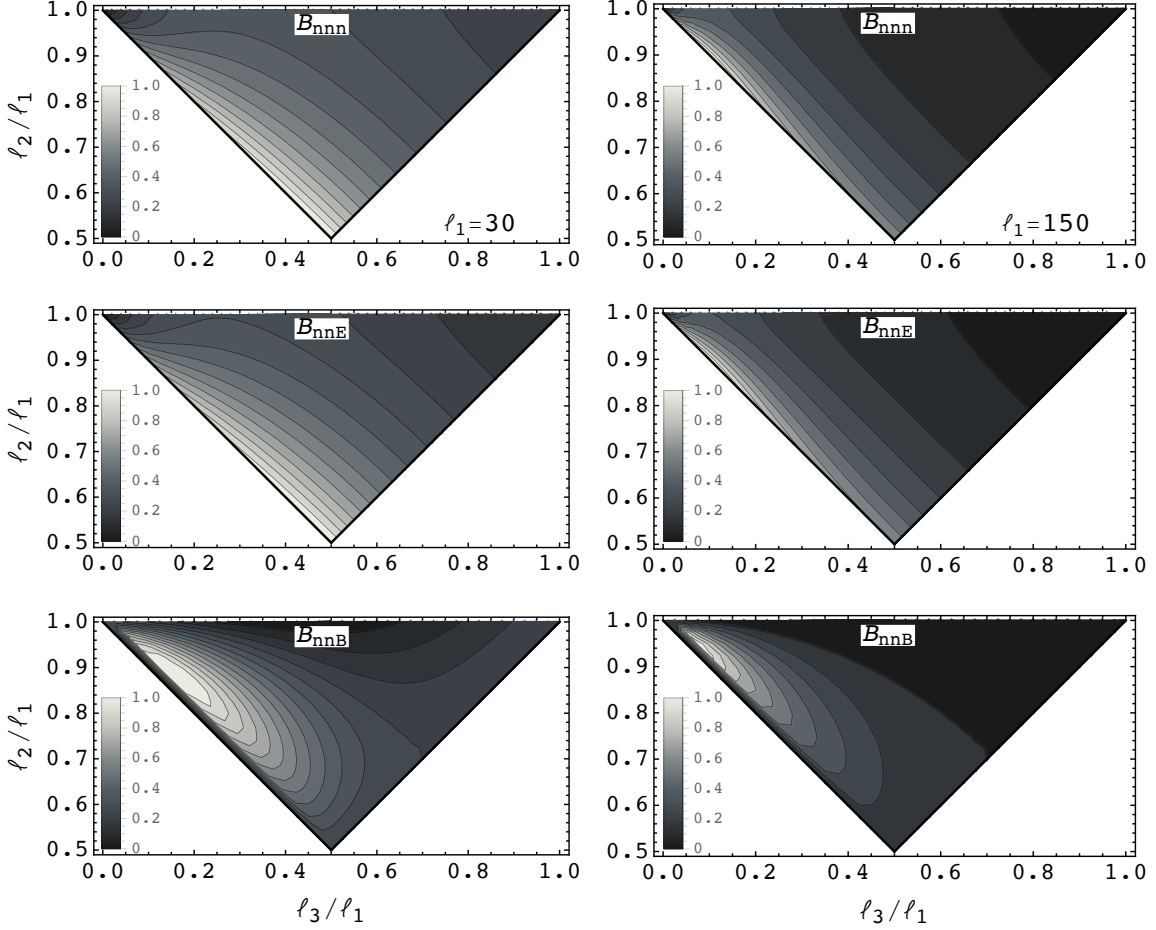


Figure 5: The angular number density and shape auto- and cross-bispectrum. Left panels show bispectra with maximal wavenumber $\ell_1 = 30$ while on the right panels it is $\ell_1 = 150$. Upper panels show the number density auto-bispectrum B_{nnn} , while the middle and lower panels show the cross-bispectrum of two number density and one shape fields in the B_{nnnE} and B_{nnnB} cross-bispectra configurations, respectively. All bispectra are normalized to its maximal amplitude configuration value. The maximal amplitudes are, typically, an order of magnitude smaller in B_{nnnB} compared to B_{nnnE} , for both $\ell_1 = 30$ and $\ell_1 = 150$ cases. Values of the bias parameters are the same as in the case of power spectra.

explained by the shape of the 3D bispectra.

Lastly, let us comment on the fact that the maximal B_{nnnB} contribution is only one order of magnitude suppressed relative to B_{nnnE} . This is in stark difference compared to the power spectrum case, where the only channel of comparison was C_ℓ^{BB} compared to C_ℓ^{EE} . There, the large suppression of C_ℓ^{BB} on large scales was caused by the fact that the leading order contribution was a one-loop result, versus the linear one for the C_ℓ^{EE} . In the case of B_{nnnE} and B_{nnnB} , this is no longer so, and both of these bispectra have non-vanishing tree-level contributions, so that the B -mode contribution is relatively much less suppressed.

6 Conclusions

In Paper I [43], we had presented an EFT expansion of galaxy intrinsic shapes, sizes and number density tracers that allows one to perform a complete prediction of three-dimensional Fourier-space statistics, i.e. power spectra up to the one-loop order and tree-level bispectra. In this work, we developed the projection formalism that relates these 3D correlators, which describe the physical dynamics of the observables, with the projected quantities that live on the 2D plane of the sky. We adopted the *flat-sky* approximation for computing the angular power and bispectra. This provides an accurate description of angular power spectrum on scales where our one-loop corrections apply. Furthermore, our results, which establish the connection between components of the 3D statistics and projected 2D statistics, are applicable to more general 3D correlators, and not just the ones predicted by the EFT of Paper I. Indeed, these projections are performed independently from the methods by which the 3D statistics is obtained and instead rely entirely on the underlying statistical symmetries (homogeneity, isotropy and parity invariance).

We presented results for the angular two- and three-point statistics of galaxy counts and shapes. The results are presented using three different bases; the helicity basis, which is the natural basis for applying the above-mentioned symmetry constraints; the electric-magnetic component basis, which is the commonly used basis in the field and in which we present our final results; and lastly, the Pauli basis that is also frequently used in the lensing community. The development of this formalism allows one to identify the forms of degeneracies taking place when projecting into the angular power spectra and bispectra, as well as which contributions survive at the tree-level bispectrum and one-loop power spectrum. In case of the power spectrum, the situation is relatively simple, and all number density and E -mode auto- and cross-correlations have contributions already at linear order. In contrast, the cross-correlations of these with the B -mode vanish to all orders as a consequence of the statistical parity invariance (in addition to the homogeneity and isotropy). The remaining B -mode auto correlation gets its leading order contribution from the one-loop mode-coupling terms. It is for this reason several orders of magnitude suppressed compared to the number density and E -mode correlators (on the scales of our interest) which, as mentioned, benefit in that respect from the leading linear order contribution. In the case of bispectra, the statistical symmetry considerations are less constraining allowing for all possible number density, E -mode and B -mode auto- and cross-correlations. However, many of these do not contribute in the tree-level PT, appearing only at higher-loop orders. This is typically the case in bispectra that correlate more than one B -mode. An interesting observation in case of B -mode contributions to the bispectrum is that it no longer is as strongly suppressed (as was the case in the power spectrum) compared to the other correlations. The reason for this is that all of the considered cross-correlations (B_{nnn} , B_{nnE} and B_{nnB}) have contributions starting at the tree-level in PT.

Assuming plausible bias parameter values, we made estimates of these correlators using the EFT results of Paper I [43], and we present several numerical results for the statistics discussed above. The current study is only qualitative and for more robust quantitative performance assessment, comparisons to simulations would be needed. On the other hand, our formalism can be readily applied to ongoing weak gravitational lensing surveys of the large-scale structure to model position-shape and shape-shape correlations, as well as three-point statistics, in a consistent and complete manner up to quasi-linear scales. Moreover, we emphasize that its potential applications are even more general: it can be applied to

any study of tensorial fields on the sky. In the future, we plan to present analogous *all-sky* derivations that can improve the accuracy of our predictions at low ℓ values, as well as predictions for configuration space correlation functions in this regime.

Acknowledgments

NEC was supported by a Royal Astronomical Society Research Fellowship for part of this project. This work is also part of the Delta ITP consortium, a program of the Netherlands Organisation for Scientific Research (NWO) that is funded by the Dutch Ministry of Education, Culture and Science (OCW). FS is supported by Starting Grant (ERC-2015-STG 678652) ‘‘GrInflaGal’’ of the European Research Council. ZV is supported by the Kavli Foundation.

A Gravitational lensing

We now provide expressions that include the gravitational lensing contribution to shapes, under the approximations stated after Eq. (3.2): first, we assume that lensing simply adds to the intrinsic shape; second, we neglect all post-Born, reduced-shear and lensing-bias corrections, so that $\gamma_{G,ij}$ can be written as the second derivative of a lensing potential, which in turn is proportional to the gravitational potential. This means that γ_G only receives helicity-0 contributions.

In the polarization basis, defined in Eq. (3.16), the angular power spectra including lensing can then be written as

$$\begin{aligned}
C_{nE}(\ell) &= \int \frac{d\chi}{\chi^2} \left[\frac{1}{2} W_n(\chi) W_g(\chi) N_0 P_{02}^{(0)}(\ell/\chi) + W_n(\chi) W_G(\chi) P_{nm}(\ell/\chi) \right], \\
C_{EE}(\ell) &= \int \frac{d\chi}{\chi^2} \left[\frac{1}{8} W_g^2(\chi) \left(2N_0^2 P_{22}^{(0)}(\ell/\chi) + N_2^2 P_{22}^{(2)}(\ell/\chi) \right) \right. \\
&\quad \left. + W_g(\chi) W_G(\chi) N_0 P_{2m}^{(0)}(\ell/\chi) + W_G^2(\chi) P_{mm}(\ell/\chi) \right], \\
C_{BB}(\ell) &= \int d\chi \frac{W_g^2(\chi)}{\chi^2} N_1^2 P_{22}^{(1)}(\ell/\chi).
\end{aligned} \tag{A.1}$$

Here,

$$W_G(\chi) = \frac{3}{2} \Omega_m H_0^2 \frac{\chi}{a} \int_{\chi}^{\infty} d\chi' W_g(\chi') \frac{\chi' - \chi}{\chi} \tag{A.2}$$

is the lensing kernel in the absence of curvature. $P_{nm}(k, z)$ is the cross-power spectrum between matter density and number counts n (which can be calculated up to 1-loop order using the EFT of biased tracers), while $P_{mm}(k, z)$ is the nonlinear matter power spectrum. $P_{2m}^{(0)}(k, z)$ is the cross-correlation between matter and the helicity-2 component of the intrinsic shape. This can be obtained in the EFT of shapes from $P_{02}^{(0)}(k, z)$ by setting all the number-count bias parameters to zero, except for b_1 which is set to 1. For explicit expressions for the EFT power spectra, we refer the reader to [43]. We defer the inclusion of the lensing contribution to bispectra statistics [e.g. 53, 63] to future work.

B Angular power spectrum

Let us assume we have a real tensor field $X_{ij}(\mathbf{r})$ such that we can identify the trace part as the simple scalar overdensity $\delta(\mathbf{r})$, while the trace-free part can be decomposed into the helicity two components $\gamma_{\pm 2}(\mathbf{r})$. In other words, we can write

$$X_{ij}(\mathbf{r}, z) = \delta(\mathbf{r}, z) \mathbf{M}_{ij}^{(0)}(\hat{\mathbf{r}}) + \gamma_{+2}(\mathbf{r}, z) \mathbf{M}_{ij}^{(+2)}(\hat{\mathbf{r}}) + \gamma_{-2}(\mathbf{r}, z) \mathbf{M}_{ij}^{(-2)}(\hat{\mathbf{r}}), \quad (\text{B.1})$$

where we have introduced (only for this section) $\mathbf{M}_{ij}^{(0)}(\hat{\mathbf{r}}) = \delta_{ij}^{\text{K}}/\sqrt{3}$. It is convenient to use this field in order to compute the relevant statistics. Moreover, we assume that the power spectrum of this field is of the form given in Eq. (2.10), i.e. we have

$$\langle X_{ij}(\mathbf{k}_1, z_1) X_{kl}(\mathbf{k}_2, z_2) \rangle = (2\pi)^3 \delta^{\text{D}}(\mathbf{k}_1 + \mathbf{k}_2) P_{ijkl}(\mathbf{k}, z_1, z_2). \quad (\text{B.2})$$

We are interested in angular statistics on the sky. Here, we focus on the flat-sky approximation results and thus we can introduce the field (see Figure 1 for coordinate setup)

$$\hat{X}_s(\boldsymbol{\ell}) = \int d^2\boldsymbol{\theta} \hat{X}_s(\boldsymbol{\theta}) e^{si(\phi_{\boldsymbol{\theta}} - \phi_{\boldsymbol{\ell}})} e^{i\boldsymbol{\ell} \cdot \boldsymbol{\theta}}, \quad (\text{B.3})$$

in analogy to Eq. (3.15), and where

$$\hat{X}_s(\boldsymbol{\theta}) = \mathbf{M}_{ij}^{(s)*}(\hat{\mathbf{n}}) \int d\chi W(\chi) X_{ij}(\chi \hat{\mathbf{n}}, \chi \boldsymbol{\theta}, z[\chi]). \quad (\text{B.4})$$

The flat-sky projected two-point function can be expressed as

$$\langle X_{ij}(\chi_1 \hat{\mathbf{n}}, \chi_1 \boldsymbol{\theta}_1) X_{kl}(\chi_2 \hat{\mathbf{n}}, \chi_2 \boldsymbol{\theta}_2) \rangle = \int \frac{d^3k}{(2\pi^3)} P_{ijkl}(\mathbf{k}) e^{-i(\chi_2 - \chi_1) \hat{\mathbf{n}} \cdot \mathbf{k} - i(\chi_2 \boldsymbol{\theta}_2 - \chi_1 \boldsymbol{\theta}_1) \cdot \mathbf{k}}, \quad (\text{B.5})$$

where

$$\begin{aligned} \langle X_{s_1}(\boldsymbol{\theta}_1) X_{s_2}^*(\boldsymbol{\theta}_2) \rangle &= \mathbf{M}_{ij}^{(s_1)*}(\hat{\mathbf{n}}) \mathbf{M}_{kl}^{(s_2)}(\hat{\mathbf{n}}) \int d\chi_1 d\chi_2 W(\chi_1) W(\chi_2) \\ &\quad \times \int \frac{d^3k}{(2\pi^3)} P_{ijkl}(\mathbf{k}) e^{-i(\chi_2 - \chi_1) \hat{\mathbf{n}} \cdot \mathbf{k} - i(\chi_2 \boldsymbol{\theta}_2 - \chi_1 \boldsymbol{\theta}_1) \cdot \mathbf{k}}. \end{aligned} \quad (\text{B.6})$$

It is convenient to setup the coordinate frame so that $k_{\parallel} = \hat{\mathbf{n}} \cdot \mathbf{k}$ and $\mathbf{k}_{\perp} = \mathbf{k} - k_{\parallel} \hat{\mathbf{n}}$, and using the variables $\chi_{2,1} = \chi \pm \frac{1}{2} \Delta\chi$. This gives us

$$\begin{aligned} &\int d\chi_1 d\chi_2 W(\chi_1) W(\chi_2) \int \frac{d^3k}{(2\pi^3)} P_{ijkl}(\mathbf{k}) e^{-i(\chi_2 - \chi_1) \hat{\mathbf{n}} \cdot \mathbf{k} - i(\chi_2 \boldsymbol{\theta}_2 - \chi_1 \boldsymbol{\theta}_1) \cdot \mathbf{k}} \\ &= \int d\chi d\Delta\chi W(\chi + \frac{1}{2} \Delta\chi) W(\chi - \frac{1}{2} \Delta\chi) \\ &\quad \times \int \frac{dk_{\parallel} d^2\mathbf{k}_{\perp}}{(2\pi)^3} P_{ijkl}(k_{\parallel} \hat{\mathbf{n}} + \mathbf{k}_{\perp}) e^{-ik_{\parallel} \Delta\chi - i\chi(\boldsymbol{\theta}_2 - \boldsymbol{\theta}_1) \cdot \mathbf{k}_{\perp} - i\frac{1}{2} \Delta\chi(\boldsymbol{\theta}_2 + \boldsymbol{\theta}_1) \cdot \mathbf{k}_{\perp}} \end{aligned} \quad (\text{B.7})$$

To further simplify the calculation note that the leading wavenumber k modes that can contribute to the integral are those ones with small $k_{\parallel} = \hat{\mathbf{n}} \cdot \mathbf{k}$, so that $k_{\parallel} \ll 1/(\chi\theta)$. Since we work in the small-angle approximation, we have $1/(\chi\theta) \gg 1/\chi$ and thus modes with longitudinal wavenumber k_{\parallel} much larger than $1/\chi$ do not give rise to angular correlations

because of cancellations along the line of sight. Only modes with k_{\parallel} similar to $1/\chi$ lead to angular correlations. The relevant transverse wavenumbers $1/(\chi\theta)$ are thus much larger than the relevant longitudinal wavenumbers, and we can set the argument of the spherical components of the tensor power spectrum to

$$P_{\ell\ell'}^{(m)}(k) = P_{\ell\ell'}^{(m)}(k) \left(\sqrt{k_{\parallel} + k_{\perp}} \right) \approx P_{\ell\ell'}^{(m)}(k_{\perp}), \quad (\text{B.8})$$

from which it follows that

$$P_{ijkl}(\mathbf{k}) = P_{ijkl}(k_{\parallel}\hat{\mathbf{n}} + \mathbf{k}_{\perp}) \approx P_{ijkl}(\mathbf{k}_{\perp}). \quad (\text{B.9})$$

We can now integrate over k_{\parallel} which gives us the delta function that sets $\Delta\chi = 0$ and

$$\begin{aligned} \int d\chi_1 d\chi_2 W(\chi_1)W(\chi_2) \int \frac{d^3k}{(2\pi^3)} P_{ijkl}(\mathbf{k}) e^{-i(\chi_2 - \chi_1)\hat{\mathbf{n}}\cdot\mathbf{k} - i(\chi_2\theta_2 - \chi_1\theta_1)\cdot\mathbf{k}} \\ \approx \int d\chi [W(\chi)]^2 \int \frac{d^2\mathbf{k}_{\perp}}{(2\pi)^2} P_{ijkl}(\mathbf{k}_{\perp}) e^{-i\chi(\theta_2 - \theta_1)\cdot\mathbf{k}_{\perp}}. \end{aligned} \quad (\text{B.10})$$

This allows us to compute the flat-sky projected angular power spectrum. Using the definition in Eq. (B.3) and the expression above we have

$$\begin{aligned} \langle \hat{X}_{s_1}(\boldsymbol{\ell}_1) \hat{X}_{s_2}^*(\boldsymbol{\ell}_2) \rangle &= \int d^2\boldsymbol{\theta}_1 d^2\boldsymbol{\theta}_2 \langle \hat{X}_{s_1}(\boldsymbol{\theta}_1) \hat{X}_{s_2}^*(\boldsymbol{\theta}_2) \rangle e^{s_1 i(\phi_{\theta_1} - \phi_{\ell_1}) - s_2 i(\phi_{\theta_2} - \phi_{\ell_2})} e^{i\boldsymbol{\ell}_1\cdot\boldsymbol{\theta}_1 - i\boldsymbol{\ell}_2\cdot\boldsymbol{\theta}_2} \\ &\approx (2\pi)^2 \delta^{\text{D}}(\boldsymbol{\ell}_1 - \boldsymbol{\ell}_2) \int d\chi \frac{[W(\chi)]^2}{\chi^2} \widetilde{\mathbf{M}}_{ij}^{(s_1)*}(\hat{\mathbf{n}}) \widetilde{\mathbf{M}}_{kl}^{(s_2)}(\hat{\mathbf{n}}) P_{ijkl}(\boldsymbol{\ell}_2/\chi). \end{aligned} \quad (\text{B.11})$$

We also used the fact that

$$\int d^2\boldsymbol{\theta} \mathbf{M}_{ij}^{(s)}(\hat{\mathbf{n}}) e^{-si(\phi_{\theta} - \phi_{\ell})} e^{-i\boldsymbol{\ell}\cdot\boldsymbol{\theta}} = (2\pi)^2 \delta^{\text{D}}(\boldsymbol{\ell}) \widetilde{\mathbf{M}}_{ij}^{(s)}(\hat{\mathbf{n}}). \quad (\text{B.12})$$

Given the decomposition of P_{ijkl} given in Eq. (2.10) we have

$$\begin{aligned} \widetilde{\mathbf{M}}_{ij}^{(s_1)*}(\hat{\mathbf{n}}) \widetilde{\mathbf{M}}_{kl}^{(s_2)}(\hat{\mathbf{n}}) P_{ijkl}(\boldsymbol{\ell}_2/\chi) &= \frac{1}{|s_1|!|s_2|!} \left(N_0^2 P_{|s_1||s_2|}^{(0)}(\boldsymbol{\ell}_2/\chi) \right. \\ &\quad \left. + s_1 s_2 N_1^2 P_{|s_1||s_2|}^{(1)}(\boldsymbol{\ell}_2/\chi) + \frac{(s_1 s_2)^2}{32} N_2^2 P_{|s_1||s_2|}^{(2)}(\boldsymbol{\ell}_2/\chi) \right). \end{aligned} \quad (\text{B.13})$$

Using the definition of flat-sky angular power spectrum

$$\langle \hat{X}_{s_1}(\boldsymbol{\ell}_1) \hat{X}_{s_2}(\boldsymbol{\ell}_2) \rangle = (2\pi)^2 \delta^{\text{D}}(\boldsymbol{\ell}_1 + \boldsymbol{\ell}_2) C_{s_1 s_2}(\boldsymbol{\ell}_1), \quad (\text{B.14})$$

we arrive at the final expression:

$$\begin{aligned} C_{s_1 s_2}(\boldsymbol{\ell}) &= \frac{1}{|s_1|!|s_2|!} \int d\chi \frac{[W(\chi)]^2}{\chi^2} \left(N_0^2 P_{|s_1||s_2|}^{(0)}(\boldsymbol{\ell}/\chi) + s_1 s_2 N_1^2 P_{|s_1||s_2|}^{(1)}(\boldsymbol{\ell}/\chi) \right. \\ &\quad \left. + \frac{(s_1 s_2)^2}{32} N_2^2 P_{|s_1||s_2|}^{(2)}(\boldsymbol{\ell}/\chi) \right), \end{aligned} \quad (\text{B.15})$$

where the normalization constants $N_{0,1,2} = \{\sqrt{3/2}, \sqrt{1/2}, 1\}$ originate from the basis $\mathbf{Y}_{ij}^{(m)}$, introduced in Eq. (2.7). Since all the components of the $C_{s_1 s_2}$ angular power spectra are real, we have

$$\langle \hat{X}_{s_1}(\boldsymbol{\ell}_1) \hat{X}_{s_2}^*(\boldsymbol{\ell}_2) \rangle = \langle \hat{X}_{s_1}^*(\boldsymbol{\ell}_1) \hat{X}_{s_2}(\boldsymbol{\ell}_2) \rangle. \quad (\text{B.16})$$

C Angular bispectrum

To obtain the flat-sky expressions for the angular bispectrum we combine Eqs. (B.3)–(B.4) to get

$$\begin{aligned}
\hat{X}_s(\boldsymbol{\ell}) &= \int d\chi W(\chi) \int d^2\boldsymbol{\theta} \mathbf{M}_{ij}^{(s)*}(\hat{\mathbf{n}}) X_{ij}(\chi\hat{\mathbf{n}}, \chi\boldsymbol{\theta}, z[\chi]) e^{si(\phi_\theta - \phi_\ell)} e^{i\boldsymbol{\ell}\cdot\boldsymbol{\theta}}, \\
&= \int d\chi W(\chi) \int d^2\boldsymbol{\theta} \mathbf{M}_{ij}^{(s)*}(\hat{\mathbf{n}}) e^{si(\phi_\theta - \phi_\ell)} e^{i\boldsymbol{\ell}\cdot\boldsymbol{\theta}} \int \frac{dk_\parallel d^2k_\perp}{(2\pi)^3} X_{ij}(\mathbf{k}, z[\chi]) e^{-i\chi k_\parallel - i\chi \mathbf{k}_\perp \cdot \boldsymbol{\theta}} \\
&= \int d\chi W(\chi) \int \frac{dk_\parallel d^2k_\perp}{2\pi} e^{-i\chi k_\parallel} \delta^D(\boldsymbol{\ell} - \chi \mathbf{k}_\perp) \widetilde{\mathbf{M}}_{ij}^{(s)*}(\hat{\mathbf{n}}) X_{ij}(k_\parallel \hat{\mathbf{n}}, \mathbf{k}_\perp, z[\chi]) \\
&= \int d\chi \frac{W(\chi)}{\chi^2} \int \frac{dk_\parallel}{2\pi} e^{-i\chi k_\parallel} \widetilde{\mathbf{M}}_{ij}^{(s)*}(\hat{\mathbf{n}}) X_{ij}(k_\parallel \hat{\mathbf{n}}, \boldsymbol{\ell}/\chi, z[\chi]).
\end{aligned} \tag{C.1}$$

Using the definition of the 3D bispectrum given in Eq. (2.12), and the same set of approximations given in appendix B (e.g. $k_\parallel \ll k_\perp$), we have

$$\begin{aligned}
&\int \frac{dk_{\parallel,123}}{(2\pi)^3} e^{-i\sum_l \chi_l k_{\parallel,l}} \langle X_{ij}(k_{\parallel,1}, \boldsymbol{\ell}_1/\chi_1, z_1) X_{nm}(k_{\parallel,2}, \boldsymbol{\ell}_2/\chi_2, z_2) X_{rs}(k_{\parallel,3}, \boldsymbol{\ell}_3/\chi_3, z_3) \rangle \\
&= \chi_3^2 \delta^D(\chi_1 - \chi_3) \delta^D(\chi_2 - \chi_3) (2\pi)^2 \delta^D(\boldsymbol{\ell}_1 + \boldsymbol{\ell}_2 + \boldsymbol{\ell}_3) B_{ijnmrs}(\boldsymbol{\ell}_1/\chi_1, \boldsymbol{\ell}_2/\chi_2, \boldsymbol{\ell}_3/\chi_3).
\end{aligned} \tag{C.2}$$

Using the definition of flat-sky angular bispectrum

$$\langle \hat{X}_{s_1}(\boldsymbol{\ell}_1) \hat{X}_{s_2}(\boldsymbol{\ell}_2) \hat{X}_{s_3}(\boldsymbol{\ell}_3) \rangle = (2\pi)^2 \delta^D(\boldsymbol{\ell}_1 + \boldsymbol{\ell}_2 + \boldsymbol{\ell}_3) B_{s_1 s_2 s_3}(\boldsymbol{\ell}_1, \boldsymbol{\ell}_2, \boldsymbol{\ell}_3), \tag{C.3}$$

we have

$$B_{s_1 s_2 s_3}(\boldsymbol{\ell}_1, \boldsymbol{\ell}_2, \boldsymbol{\ell}_3) = \int d\chi \frac{[W(\chi)]^3}{\chi^4} \widetilde{\mathbf{M}}_{ij}^{(s_1)*}(\hat{\mathbf{n}}) \widetilde{\mathbf{M}}_{nm}^{(s_2)*}(\hat{\mathbf{n}}) \widetilde{\mathbf{M}}_{rs}^{(s_3)*}(\hat{\mathbf{n}}) B_{ijnmrs}(\tilde{\boldsymbol{\ell}}_1, \tilde{\boldsymbol{\ell}}_2, \tilde{\boldsymbol{\ell}}_3), \tag{C.4}$$

where $\tilde{\boldsymbol{\ell}}_i = \boldsymbol{\ell}_i/\chi$. Under the assumptions that $k_\parallel \ll k_\perp$ we can evaluate the basis $\mathbf{Y}^{(q)}$ from Eq. (2.7) by setting the $\hat{\mathbf{k}}$ so that it lays on one of the z planes (see figure 1). We thus have

$$\widetilde{\mathbf{M}}_{ij}^{(s)*}(\hat{\mathbf{n}}) \mathbf{Y}_{ij}^{(q)}(\hat{\mathbf{n}}) = i^{s-2q} c_{s,q}, \tag{C.5}$$

where $c_{s,q}$ are the following coefficients

$c_{s,q}$	-2	-1	0	+1	+2
+2	1/4	$i/2$	$-1/2\sqrt{3/2}$	$-i/2$	1/4
-2	1/4	$-i/2$	$-1/2\sqrt{3/2}$	$i/2$	1/4

Using these results and Eq. (2.10), one can also recover the angular power spectrum results given in Eq. (4.3) and derived explicitly in appendix B. However, in this section we focus on the angular bispectrum results. Using the 3D bispectrum decompositions as given

in section Eq. (2.14) we have

$$\begin{aligned}
B_{\text{nnn}}(\ell_1, \ell_2, \ell_3) &= \int d\chi \frac{[W_n(\chi)]^3}{\chi^4} B_{000}^{(0)}(\tilde{\ell}_1, \tilde{\ell}_2, \tilde{\ell}_3), \tag{C.6} \\
B_{\text{nns}_3}(\ell_1, \ell_2, \ell_3) &= \frac{1}{2} \int d\chi \frac{[W_n(\chi)]^2 W_g(\chi)}{\chi^4} \left[N_0 B_{002}^{(0)} - i s_3 \sqrt{2} N_1 B_{002}^{(1)} - N_2 B_{002}^{(2)} \right] (\tilde{\ell}_1, \tilde{\ell}_2, \tilde{\ell}_3), \\
B_{\text{ns}_2 s_3}(\ell_1, \ell_2, \ell_3) &= \frac{1}{8} \int d\chi \frac{W_n(\chi) [W_g(\chi)]^2}{\chi^4} \left[2N_0^2 B_{022}^{(0,0)} + 2s_2 s_3 N_1^2 \left(B_{022}^{(-1,1)} - B_{022}^{(1,1)} \right) \right. \\
&\quad - i 2\sqrt{2} N_0 N_1 \left(s_3 B_{022}^{(0,1)} + s_2 B_{022}^{(1,0)} \right) \\
&\quad + i\sqrt{2} N_1 N_2 \left(s_2 B_{022}^{(1,2)} + s_3 B_{022}^{(2,1)} + s_3 B_{022}^{(-2,1)} + s_2 B_{022}^{(1,-2)} \right) \\
&\quad \left. - 2N_0 N_2 B_{022}^{\{\{0,2\}\}} + N_2^2 \left(B_{022}^{(-2,2)} + B_{022}^{(2,2)} \right) \right] (\tilde{\ell}_1, \tilde{\ell}_2, \tilde{\ell}_3), \\
B_{s_1 s_2 s_3}(\ell_1, \ell_2, \ell_3) &= \frac{1}{32} \int d\chi \frac{[W_g(\chi)]^3}{\chi^4} \left[4N_0^3 B_{222}^{(0,0,0)} - 4N_0^2 N_2 B_{222}^{\{\{0,0,2\}\}} \right. \\
&\quad - N_2^3 \left(B_{222}^{\{\{-2,2,2\}\}} + B_{222}^{(2,2,2)} \right) \\
&\quad + 4N_0 N_1^2 \left(s_2 s_3 \left(B_{222}^{(0,-1,1)} - B_{222}^{(0,1,1)} \right) + 2 \text{ cyc.} \right) \\
&\quad + 2N_0 N_2^2 \left(B_{222}^{\{\{0,-2,2\}\}} + B_{222}^{\{\{0,2,2\}\}} \right) \\
&\quad + 2N_1^2 N_2 \left(s_1 s_2 \left(B_{222}^{(1,1,2)} + B_{222}^{(1,1,-2)} - B_{222}^{\{\{-1,1,2\}\}} \right) + 2 \text{ cyc.} \right) \\
&\quad - i 4\sqrt{2} N_0^2 N_1 \left(s_3 B_{222}^{(0,0,1)} + 2 \text{ cyc.} \right) \\
&\quad - i 2\sqrt{2} s_1 s_2 s_3 N_1^3 \left(B_{222}^{\{\{-1,1,1\}\}} - B_{222}^{(1,1,1)} \right) \\
&\quad - i\sqrt{2} N_1 N_2^2 \left(s_3 \left(B_{222}^{\{\{-2,2\},1\}} + B_{222}^{(2,2,1)} - B_{222}^{(2,2,-1)} \right) + 2 \text{ cyc.} \right) \\
&\quad \left. + i 2\sqrt{2} N_1 N_2 N_3 \left(s_3 \left(B_{222}^{\{\{0,-2\},1\}} + B_{222}^{\{\{0,2\},1\}} \right) + 2 \text{ cyc.} \right) \right] (\tilde{\ell}_1, \tilde{\ell}_2, \tilde{\ell}_3).
\end{aligned}$$

Where $(\{a, b, c\})$ notation is used and we understand that the summation over all the non-trivial index permutations should be performed. Above we also used the bispectrum parity relation given in Eq. (2.15) to reduce the number of independent terms. Each of the cross angular bispectra has contributions from different helicities, which give rise to the terms in the integrand. Depending on the number of helicity two fields in the angular bispectrum number of terms in the integrand varies from three for the density-density-shear (002) bispectrum, six for the density-shear-shear (022) bispectrum and ten for the shear-shear-shear (222). These multiplicities correspond to the number of combinations with repetition for the helicity of the shear field.

In Paper I [43] we gave the explicit bispectrum results for biased tracers up to the tree-level (leading order) PT. In that case only, few of the terms above survive given that leading order fields carry only helicity zero contribution. In other words, only single non-zero helicity

terms survive and we have

$$\begin{aligned}
B_{\text{nnn}}^{\text{LO}}(\ell_1, \ell_2, \ell_3) &= \int d\chi \frac{[W_n(\chi)]^3}{\chi^4} B_{000}^{(0)}(\tilde{\ell}_1, \tilde{\ell}_2, \tilde{\ell}_3), \tag{C.7} \\
B_{\text{nn}s_3}^{\text{LO}}(\ell_1, \ell_2, \ell_3) &= \frac{1}{2} \int d\chi \frac{[W_n(\chi)]^2 W_g(\chi)}{\chi^4} \left[N_0 B_{002}^{(0)} - i s_3 \sqrt{2} N_1 B_{002}^{(1)} - N_2 B_{002}^{(2)} \right] (\tilde{\ell}_1, \tilde{\ell}_2, \tilde{\ell}_3), \\
B_{\text{ns}_2 s_3}^{\text{LO}}(\ell_1, \ell_2, \ell_3) &= \frac{1}{4} N_0 \int d\chi \frac{W_n(\chi) [W_g(\chi)]^2}{\chi^4} \left[N_0 B_{022}^{(0,0)} - N_2 B_{022}^{\{0,2\}} \right. \\
&\quad \left. - i \sqrt{2} N_1 (s_3 B_{022}^{(0,1)} + s_2 B_{022}^{(1,0)}) \right] (\tilde{\ell}_1, \tilde{\ell}_2, \tilde{\ell}_3), \\
B_{s_1 s_2 s_3}^{\text{LO}}(\ell_1, \ell_2, \ell_3) &= \frac{1}{8} N_0^2 \int d\chi \frac{[W_g(\chi)]^3}{\chi^4} \left[N_0 B_{222}^{(0,0,0)} - N_0^2 N_2 B_{222}^{\{0,0,2\}} \right. \\
&\quad \left. - i \sqrt{2} N_0^2 N_1 (s_3 B_{222}^{(0,0,1)} + 2 \text{cyc.}) \right] (\tilde{\ell}_1, \tilde{\ell}_2, \tilde{\ell}_3).
\end{aligned}$$

These results for $B_{\text{nn}s_3}^{\text{LO}}$ agree with the projections used in Paper I [43] to decompose the bispectrum at tree-level in PT.

References

- [1] C. Heymans et al., *CFHTLenS tomographic weak lensing cosmological parameter constraints: Mitigating the impact of intrinsic galaxy alignments*, *Mon. Not. Roy. Astron. Soc.* **432** (2013) 2433, [[1303.1808](#)].
- [2] M. J. Jee, J. A. Tyson, M. D. Schneider, D. Wittman, S. Schmidt and S. Hilbert, *Cosmic shear results from the deep lens survey - I: Joint constraints on omega_m and sigma_8 with a two-dimensional analysis*, *Astrophys. J.* **765** (2013) 74, [[1210.2732](#)].
- [3] E. M. Huff, T. Eifler, C. M. Hirata, R. Mandelbaum, D. Schlegel and U. Seljak, *Seeing in the dark. 2. Cosmic shear in the Sloan Digital Sky Survey*, *Mon. Not. Roy. Astron. Soc.* **440** (2014) 1322–1344, [[1112.3143](#)].
- [4] H. Hildebrandt et al., *KiDS-450: Cosmological parameter constraints from tomographic weak gravitational lensing*, *Mon. Not. Roy. Astron. Soc.* **465** (2017) 1454, [[1606.05338](#)].
- [5] DES collaboration, M. A. Troxel et al., *Dark Energy Survey Year 1 results: Cosmological constraints from cosmic shear*, *Phys. Rev.* **D98** (2018) 043528, [[1708.01538](#)].
- [6] H. Hildebrandt et al., *KiDS+VIKING-450: Cosmic shear tomography with optical+infrared data*, [[1812.06076](#)].
- [7] S. Joudaki et al., *KiDS+VIKING-450 and DES-Y1 combined: Cosmology with cosmic shear*, [[1906.09262](#)].
- [8] R. Mandelbaum, C. M. Hirata, M. Ishak, U. Seljak and J. Brinkmann, *Detection of large scale intrinsic ellipticity-density correlation from the sloan digital sky survey and implications for weak lensing surveys*, *Mon. Not. Roy. Astron. Soc.* **367** (2006) 611–626, [[astro-ph/0509026](#)].
- [9] C. M. Hirata, R. Mandelbaum, M. Ishak, U. Seljak, R. Nichol, K. A. Pimbblet et al., *Intrinsic galaxy alignments from the 2SLAQ and SDSS surveys: Luminosity and redshift scalings and implications for weak lensing surveys*, *Mon. Not. Roy. Astron. Soc.* **381** (2007) 1197–1218, [[astro-ph/0701671](#)].
- [10] T. Okumura, Y. P. Jing and C. Li, *Intrinsic Ellipticity Correlation of SDSS Luminous Red Galaxies and Misalignment with their Host Dark Matter Halos*, *Astrophys. J.* **694** (2009) 214–221, [[0809.3790](#)].

- [11] S. Singh, R. Mandelbaum and S. More, *Intrinsic alignments of SDSS-III BOSS LOWZ sample galaxies*, *Mon. Not. Roy. Astron. Soc.* **450** (2015) 2195–2216, [[1411.1755](#)].
- [12] N. E. Chisari, C. Dvorkin and F. Schmidt, *Can weak lensing surveys confirm BICEP2?*, *Phys. Rev.* **D90** (2014) 043527, [[1406.4871](#)].
- [13] F. Schmidt, N. E. Chisari and C. Dvorkin, *Imprint of inflation on galaxy shape correlations*, *JCAP* **1510** (2015) 032, [[1506.02671](#)].
- [14] N. E. Chisari, C. Dvorkin, F. Schmidt and D. Spergel, *Multitracing Anisotropic Non-Gaussianity with Galaxy Shapes*, *Phys. Rev.* **D94** (2016) 123507, [[1607.05232](#)].
- [15] K. Akitsu, T. Kurita, T. Nishimichi, M. Takada and S. Tanaka, *Imprint of anisotropic primordial non-Gaussianity on halo intrinsic alignments in simulations*, [2007.03670](#).
- [16] P. Catelan, M. Kamionkowski and R. D. Blandford, *Intrinsic and extrinsic galaxy alignment*, *Mon. Not. Roy. Astron. Soc.* **320** (2001) L7–L13, [[astro-ph/0005470](#)].
- [17] S. Bridle and L. King, *Dark energy constraints from cosmic shear power spectra: impact of intrinsic alignments on photometric redshift requirements*, *New J. Phys.* **9** (2007) 444, [[0705.0166](#)].
- [18] M. D. Schneider and S. Bridle, *A halo model for intrinsic alignments of galaxy ellipticities*, *Mon. Not. Roy. Astron. Soc.* **402** (2010) 2127, [[0903.3870](#)].
- [19] B. Joachimi, E. Semboloni, P. E. Bett, J. Hartlap, S. Hilbert, H. Hoekstra et al., *Intrinsic galaxy shapes and alignments I: Measuring and modelling COSMOS intrinsic galaxy ellipticities*, *Mon. Not. Roy. Astron. Soc.* **431** (2013) 477–492, [[1203.6833](#)].
- [20] B. Joachimi, E. Semboloni, S. Hilbert, P. E. Bett, J. Hartlap, H. Hoekstra et al., *Intrinsic galaxy shapes and alignments II: Modelling the intrinsic alignment contamination of weak lensing surveys*, [1305.5791](#).
- [21] A. Heavens, A. Refregier and C. Heymans, *Intrinsic correlation of galaxy shapes: Implications for weak lensing measurements*, *Mon. Not. Roy. Astron. Soc.* **319** (2000) 649, [[astro-ph/0005269](#)].
- [22] R. G. Crittenden, P. Natarajan, U.-L. Pen and T. Theuns, *Spin induced galaxy alignments and their implications for weak lensing measurements*, *Astrophys. J.* **559** (2001) 552–571, [[astro-ph/0009052](#)].
- [23] J. Mackey, M. J. White and M. Kamionkowski, *Theoretical estimates of intrinsic galaxy alignment*, *Mon. Not. Roy. Astron. Soc.* **332** (2002) 788, [[astro-ph/0106364](#)].
- [24] A. Kiessling et al., *Galaxy Alignments: Theory, Modelling & Simulations*, *Space Sci. Rev.* **193** (2015) 67–136, [[1504.05546](#)].
- [25] S. Codis, R. Gavazzi, Y. Dubois, C. Pichon, K. Benabed, V. Desjacques et al., *Intrinsic alignment of simulated galaxies in the cosmic web: implications for weak lensing surveys*, *Mon. Not. Roy. Astron. Soc.* **448** (2015) 3391–3404, [[1406.4668](#)].
- [26] N. E. Chisari, S. Codis, C. Laigle, Y. Dubois, C. Pichon, J. Devriendt et al., *Intrinsic alignments of galaxies in the Horizon-AGN cosmological hydrodynamical simulation*, *Mon. Not. Roy. Astron. Soc.* **454** (2015) 2736–2753, [[1507.07843](#)].
- [27] N. E. Chisari, C. Laigle, S. Codis, Y. Dubois, J. Devriendt, L. Miller et al., *Redshift and luminosity evolution of the intrinsic alignments of galaxies in Horizon-AGN*, *Mon. Not. Roy. Astron. Soc.* **461** (2016) 2702–2721, [[1602.08373](#)].
- [28] M. Velliscig et al., *The alignment and shape of dark matter, stellar, and hot gas distributions in the EAGLE and cosmo-OWLS simulations*, *Mon. Not. Roy. Astron. Soc.* **453** (2015) 721–738, [[1504.04025](#)].

- [29] M. Velliscig et al., *Intrinsic alignments of galaxies in the EAGLE and cosmo-OWLS simulations*, *Mon. Not. Roy. Astron. Soc.* **454** (2015) 3328–3340, [[1507.06996](#)].
- [30] A. Tenneti, R. Mandelbaum, T. Di Matteo, Y. Feng and N. Khandai, *Galaxy Shapes and Intrinsic Alignments in The MassiveBlack-II Simulation*, *Mon. Not. Roy. Astron. Soc.* **441** (2014) 470–485, [[1403.4215](#)].
- [31] A. Tenneti, S. Singh, R. Mandelbaum, T. Di Matteo, Y. Feng and N. Khandai, *Intrinsic alignments of galaxies in the MassiveBlack-II simulation: analysis of two-point statistics*, *Mon. Not. Roy. Astron. Soc.* **448** (2015) 3522–3544, [[1409.7297](#)].
- [32] A. Tenneti, R. Mandelbaum, T. Di Matteo, A. Kiessling and N. Khandai, *Galaxy shapes and alignments in the MassiveBlack-II hydrodynamic and dark matter-only simulations*, *Mon. Not. Roy. Astron. Soc.* **453** (2015) 469–482, [[1505.03124](#)].
- [33] A. Tenneti, N. Y. Gnedin and Y. Feng, *Impact of Baryonic Physics on Intrinsic Alignments*, *Astrophys. J.* **834** (2017) 169, [[1607.07140](#)].
- [34] N. E. Chisari et al., *Galaxy?halo alignments in the Horizon-AGN cosmological hydrodynamical simulation*, *Mon. Not. Roy. Astron. Soc.* **472** (2017) 1163–1181, [[1702.03913](#)].
- [35] S. Hilbert, D. Xu, P. Schneider, V. Springel, M. Vogelsberger and L. Hernquist, *Intrinsic Alignments of Galaxies in the Illustris Simulation*, *Mon. Not. Roy. Astron. Soc.* **468** (2017) 790–823, [[1606.03216](#)].
- [36] A. Taruya and T. Okumura, *Improving geometric and dynamical constraints on cosmology with intrinsic alignments of galaxies*, [2001.05962](#).
- [37] T. Kurita, M. Takada, T. Nishimichi, R. Takahashi, K. Osato and Y. Kobayashi, *Power spectrum of halo intrinsic alignments in simulations*, [2004.12579](#).
- [38] E. Krause, T. Eifler and J. Blazek, *The impact of intrinsic alignment on current and future cosmic shear surveys*, *Mon. Not. Roy. Astron. Soc.* **456** (2016) 207–222, [[1506.08730](#)].
- [39] J. Blazek, Z. Vlah and U. Seljak, *Tidal alignment of galaxies*, *JCAP* **1508** (2015) 015, [[1504.02510](#)].
- [40] J. Blazek, N. MacCrann, M. A. Troxel and X. Fang, *Beyond linear galaxy alignments*, [1708.09247](#).
- [41] D. M. Schmitz, C. M. Hirata, J. Blazek and E. Krause, *Time evolution of intrinsic alignments of galaxies*, *JCAP* **1807** (2018) 030, [[1805.02649](#)].
- [42] DES collaboration, S. Samuroff et al., *Dark Energy Survey Year 1 Results: Constraints on Intrinsic Alignments and their Colour Dependence from Galaxy Clustering and Weak Lensing*, *Mon. Not. Roy. Astron. Soc.* **489** (2019) 5453–5482, [[1811.06989](#)].
- [43] Z. Vlah, N. E. Chisari and F. Schmidt, *An EFT description of galaxy intrinsic alignments*, *JCAP* **01** (2020) 025, [[1910.08085](#)].
- [44] M. Mirbabayi, F. Schmidt and M. Zaldarriaga, *Biased Tracers and Time Evolution*, *JCAP* **1507** (2015) 030, [[1412.5169](#)].
- [45] V. Desjacques, D. Jeong and F. Schmidt, *Large-Scale Galaxy Bias*, *Phys. Rept.* **733** (2018) 1–193, [[1611.09787](#)].
- [46] J. Sakurai and J. Napolitano, *Modern Quantum Mechanics*. Addison-Wesley, 2011.
- [47] W. Hu, *Weak lensing of the CMB: A harmonic approach*, *Phys. Rev.* **D62** (2000) 043007, [[astro-ph/0001303](#)].
- [48] U. Seljak, *Measuring polarization in cosmic microwave background*, *Astrophys. J.* **482** (1997) 6, [[astro-ph/9608131](#)].

- [49] M. Zaldarriaga and U. Seljak, *An all sky analysis of polarization in the microwave background*, *Phys. Rev.* **D55** (1997) 1830–1840, [[astro-ph/9609170](#)].
- [50] W. Hu and M. J. White, *CMB anisotropies: Total angular momentum method*, *Phys. Rev.* **D56** (1997) 596–615, [[astro-ph/9702170](#)].
- [51] P. G. Castro, A. F. Heavens and T. D. Kitching, *Weak lensing analysis in three dimensions*, *Phys. Rev.* **D72** (2005) 023516, [[astro-ph/0503479](#)].
- [52] M. LoVerde and N. Afshordi, *Extended Limber Approximation*, *Phys. Rev.* **D78** (2008) 123506, [[0809.5112](#)].
- [53] M. Bartelmann and P. Schneider, *Weak gravitational lensing*, *Phys. Rept.* **340** (2001) 291–472, [[astro-ph/9912508](#)].
- [54] M. J. White, *Reducing the shear*, *Astropart. Phys.* **23** (2005) 349–354, [[astro-ph/0502003](#)].
- [55] S. Dodelson, C. Shapiro and M. J. White, *Reduced shear power spectrum*, *Phys. Rev.* **D73** (2006) 023009, [[astro-ph/0508296](#)].
- [56] F. Schmidt, E. Rozo, S. Dodelson, L. Hui and E. Sheldon, *Size Bias in Galaxy Surveys*, *Phys. Rev. Lett.* **103** (2009) 051301, [[0904.4702](#)].
- [57] F. Schmidt, E. Rozo, S. Dodelson, L. Hui and E. Sheldon, *Lensing Bias in Cosmic Shear*, *Astrophys. J.* **702** (2009) 593–602, [[0904.4703](#)].
- [58] E. Krause and C. M. Hirata, *Weak lensing power spectra for precision cosmology: Multiple-deflection, reduced shear and lensing bias corrections*, *Astron. Astrophys.* **523** (2010) A28, [[0910.3786](#)].
- [59] D. Jeong, F. Schmidt and E. Sefusatti, *Primordial Non-Gaussianity and the Statistics of Weak Lensing and other Projected Density Fields*, *Phys. Rev.* **D83** (2011) 123005, [[1104.0926](#)].
- [60] C. Chang, M. Jarvis, B. Jain, S. Kahn, D. Kirkby, A. Connolly et al., *The Effective Number Density of Galaxies for Weak Lensing Measurements in the LSST Project*, *Mon. Not. Roy. Astron. Soc.* **434** (2013) 2121, [[1305.0793](#)].
- [61] LSST SCIENCE, LSST PROJECT collaboration, P. A. Abell et al., *LSST Science Book, Version 2.0*, [0912.0201](#).
- [62] M. Biagetti and G. Orlando, *Primordial Gravitational Waves from Galaxy Intrinsic Alignments*, *JCAP* **07** (2020) 005, [[2001.05930](#)].
- [63] M. Takada and B. Jain, *Cosmological parameters from lensing power spectrum and bispectrum tomography*, *Mon. Not. Roy. Astron. Soc.* **348** (2004) 897, [[astro-ph/0310125](#)].